Heat Mass Transfer (2007) 44:229–250
DOI 10.1007/s00231-007-0244-9

ORIGINAL

Direct numerical simulation of turbulent flow and heat transfer in a square duct with natural convection

Liang-Dong Ma · Zeng-Yao Li · Wen-Quan Tao

Received: 19 October 2006 / Accepted: 2 February 2007 / Published online: 22 February 2007

Abstract In this paper, a direct numerical simulation of a fully developed turbulent flow and heat transfer are studied in a square duct with an imposed temperature difference between the vertical walls and the perfectly insulated horizontal walls. The natural convection is considered on the cross section in the duct. The numerical scheme employs a time-splitting method to integrate the three dimensional incompressible Navier-Stokes equation. The unsteady flow field was simulated at a Reynolds number of 400 based on the Mean friction velocity and the hydraulic diameter (Re_m = 6200), while the Prandtl number (Pr) is assumed 0.71. Four different Grashof numbers ($Gr = 10^4$, 10^5, 10^6 and 10^7) are considered. The results show that the secondary flow and turbulent characteristics are not affected obviously at lower Grashof number ($Gr \leq 10^5$) cases, while for the higher Grashof number cases, natural convection has an important effect, but the mean flow and mean temperature at the cross section are also affected strongly by Reynolds stresses. Compared with the laminar heat transfer at the same Grashof number, the intensity of the combined heat transfer is somewhat decreased.

List of symbols

c_p	specific heat at constant pressure (kJ/kg/K)
Gr	Grashof number, $g\beta(T_h - T_c)H^3/v^2$
g	gravitational acceleration (m/s^2)
H	width of duct (m)
i_x	unit vector in the streamwise direction
i_y	unit vector in the y-direction
Nu	Nusselt number, $Nu = q_w H/(\lambda \Delta T)$
N_y	number of grid points in the y-direction
Pr	molecular Prandtl number
q_w	the total heat transfer at the warm wall (W/m^2)
Ra	Rayleigh number, $GrPr$
Re_m	bulk mean Reynolds number, $Re_m = u_m H/v$
Re_τ	Reynolds number,$Re_\tau = u_\tau H/v$
T_c	the temperature on the cold wall (K)
T_h	the temperature on the warm wall (K)
T_0	reference temperature (K)
u, v, w	the velocity components in x-, y- and z-directions (m/s)
u_τ	friction velocity, $\sqrt{\tau_w/\rho}$
p	fluctuating pressure, $p = P/\left(\rho u_\tau^2\right)$
$\hat{p}$	dimensional fluctuating pressure (N/m^2)
x, y, z	Cartesian coordinates (m)

Greek

β	volumetric expansion coefficient (1/K)
ΔT	temperature difference, $T_h - T_c$ (K)
Θ_τ	friction temperature
θ	dimensionless temperature
λ	thermal conductivity (W/m/K)
v	kinematic viscosity (m^2/s)
ρ	density (kg/m^3)
τ_w	wall shear stress (N/m^2)
< >	ensemble average in the x-direction and in time

Subscripts

m	mean
max	maximum

L.-D. Ma · Z.-Y. Li · W.-Q. Tao (✉)
State Key Laboratory of Multiphase Flow in Power Engineering, School of Energy and Power Engineering, Xi' an Jiaotong University, Xi'an, China
e-mail: wqtao@mail.xjtu.edu.cn

rms root-mean-square
w wall
~ instantaneous variable
′ fluctuating value

Superscripts
* intermediate value

1 Introduction

Noncircular ducts are frequently occurring in the heat transfer equipment, for example, flow ducts in compact heat exchangers, cooling channels in gas turbines, and the ducts of ventilation and air condition systems. The turbulent flow field in the vicinity of a smooth corner in these ducts will be subject to a remarkable flow structure change because there have two inhomogeneous directions and exist the so-called secondary flows of second kind created by the turbulent motion, as first defined by Prandtl in 1926 [1]. These secondary flows convect momentum and scalar quantities from the center region of the duct to the wall along the corner dissectors, and away from the corners to the center along the bounding walls. The secondary flow of second kind is relatively weak, whose velocity is usually only about 2–3% of the streamwise bulk velocity in magnitude, however, their influence on wall stress distribution, heat transfer rate and transfer of passive tracers are quite significant [1].

A considerable number of experimental investigations have been carried on the turbulent flow in straight non-circular ducts. Nikuradse was perhaps the first one to observe the secondary motion in non-circular duct by flow-visualization studies [2]. The other measurements of the various aspects of the developing and fully development turbulent flow through noncircular ducts were reported by several investigators over last four decades [3–5]. A review of experimental work on turbulent flow has been given by Demuren and Rodi [2].

Several numerical calculations simulating turbulent flows in noncircular ducts have been reported in the literature. It is commonly known that the isotropic eddy-viscosity model can not predict turbulent-driven secondary flow. An algebraic stress model developed by Launder and Ying [6] and Rodi [2] was applied to the turbulent flow in a square duct. The non-linear forms of k-ε equations developed by Speziale [7] are able to predict the existence of secondary flows. Naji et.al. [8] used two explicit algebraic Reynolds stress models to accurately predict the fully turbulent flow in a straight square duct. Their predictions and DNS results obtained for a Reynolds number of 4,800 agree well, and their results show that the equilibrium assumption for the anisotropy tensor is found to be correct. Pettersson and Andersson [9] employed the elliptic relaxation approach in conjunction with second-moment closure to the fully developed turbulent flow inside a straight square duct. The results are compared favourably with the reference DNS data, except that the strength of the turbulence-induced secondary flows is significantly underpredicted. Generally speaking, all these models can predict the secondary flow on the cross-section in the square duct, but the comparison of predicted turbulent quantities with experimental data is not completely satisfactory, because the origin of the secondary motion in these models depends on the empirical models. Recently, in order to reveal the physical mechanisms and explain the origin of secondary flow in non-circular duct, the large eddy simulation (LES) and direct numerical simulation are used to predict the turbulent flow in the square duct. Kajishima and Miyake [10], Madabhushi and Vanka [11], Su and Friedrich [12] performed the LES for studying the turbulent flow. These simulations correctly predicted the existence of secondary flows and their effects on the mean flow and the turbulence statistics. In reference [13], a priori tests of two dynamic subgrid-scale turbulence models have been performed for the case of turbulent incompressible flow in a straight duct of square cross-section. The grid requirements are very demanding in LES. Especially, the resolution in the boundary layer has to be fine and increases with Reynolds number. To limit the number of grid points in boundary layer, detached eddy simulation (DES) is used. Viswanathan and Tafti [14] employed DES to investigate turbulent flow and heat transfer in a two-pass internal cooling duct. Compared with the LES, the DNS is able to predict the secondary flow in a straight duct with square cross section better because it does not need any turbulence models and can reveal valuable information on the turbulence structures. Gavrilakis [15] carried on the direct numerical simulation of the fully developed turbulent flow thorough a straight duct of square cross-section, and the Reynolds number based on the bulk velocity and hydraulic diameter was 4,410, providing a detailed description of the mean flow in the transverse plane and turbulence statistics along the wall bisector. Latterly, Huser and Biringen [16] also performed a DNS of the square duct flow, providing detailed turbulence statistics, the characteristics of the Reynolds-averaged flow field, and detailed description of the corner influence on turbulence statistics and on the origin of the secondary flows of the second kind in the fully developed turbulent flow. To the multiphase flow, Sharma and Phares [17] empolyed DNS to investigate the role of the secondary flows in the transport and dispersion of particles suspended in a turbulent square duct flow. These researches were focused upon the fluid dynamic features and the heat transfer was not considered. Piller and Nobile [1] adopt DNS for studying both the turbulent velocity and the temperature fields in a square duct with an imposed temperature difference between the horizontal walls and the vertical walls are assumed perfectly insulated. Buoyancy forces are neglected in study, so that the temperature field behaves like a passive scalar in that the fluid temperature does not affect the flow field at all. The results show that the secondary flow does not affect dramatically the friction factor and the Nusselt number with respect to the plane channel flow but the distributions of local heat flux and shear-stress at the walls are highly non-uniform. It is also shown that the eddy-diffusivity approach is capable to reproduce well the turbulent heat flux.

The objective of this work is to perform a DNS of the square duct flow with the natural convection. Direct numerical simulation was adopted to study both the velocity and the temperature field in the fully developed turbulent square duct. A constant temperature difference is imposed between the vertical walls, while the horizontal walls are assumed perfectly insulated. The Reynolds number based on the friction velocity and hydraulic diameter is 400, and the Prandtl number is 0.71. Four different Grashof numbers ($Gr = 10^4$, 10^5, 10^6 and 10^7) are considered, so that, the flow and temperature field are controlled by both the Reynolds stresses and buoyancy body force on the cross section in the square duct. The MPI parallel programming language was used to speed-up the calculations. Maximal CPU number is up to eight in the DNS, obtaining satisfactory performances. The simulation results provide a database in which turbulence statistics and the characteristics of the Reynolds-averaged flow field are included, and a detailed description of the Reynolds stresses' spatial distribution. By analyzing the spatial distribution of the all terms of streamwise momentum and energy equation, it is found that the Reynolds stresses gradient is dominant for lower Gr number ($Gr \le 10^5$), while the contribution from mean convection becomes significant for higher Gr number.

2 Problem definition and scales

The geometry and coordinate system are shown in Fig. 1. In the present calculations the Boussinesq approximation is adopted, so the physical properties of the fluid ($Pr = 0.7$) are assumed to be constant. Only the density in the buoyancy term of the vertical direction momentum equation is a variable of temperature and the Boussinesq assumption is adopted to relate the density and temperature [18]. The governing equations are the three-dimensional, time-dependent Navier–Stokes equations, the continuity equation and energy equation. They are expressed in the following dimensionless form in the Cartesian coordinates [18]

$$\frac{D\tilde{u}}{Dt} = -\frac{\partial \tilde{p}}{\partial x} + \frac{1}{Re_\tau}\nabla^2\tilde{u} + 4 \tag{1}$$

$$\frac{D\tilde{v}}{Dt} = -\frac{\partial}{\partial y}\left(\tilde{p} + \frac{gy}{u_\tau^2}\right) + \frac{1}{Re_\tau}\nabla^2\tilde{v} + \frac{Gr}{Re_\tau^2}\left(\tilde{\theta} + \frac{T_c - T_0}{\Delta T}\right) \tag{2}$$

$$\frac{D\tilde{w}}{Dt} = -\frac{\partial \tilde{p}}{\partial z} + \frac{1}{Re_\tau}\nabla^2\tilde{w} \tag{3}$$

$$\frac{\partial \tilde{u}}{\partial x} + \frac{\partial \tilde{v}}{\partial y} + \frac{\partial \tilde{w}}{\partial z} = 0 \tag{4}$$

$$\frac{D\tilde{\theta}}{Dt} = \frac{1}{PrRe_\tau}\nabla^2\tilde{\theta} \tag{5}$$

where the mean friction velocity, u_τ, the duct width, H, and the temperature difference, ΔT (= T_h–T_c), are used as the velocity, length and temperature scales, respectively. T_0 is the reference temperature, here, $T_0 = T_c$, i.e., the temperature of the cold wall. And $\tilde{u}, \tilde{v}$ and $\tilde{w}$ are instantaneous dimensionless velocity in the

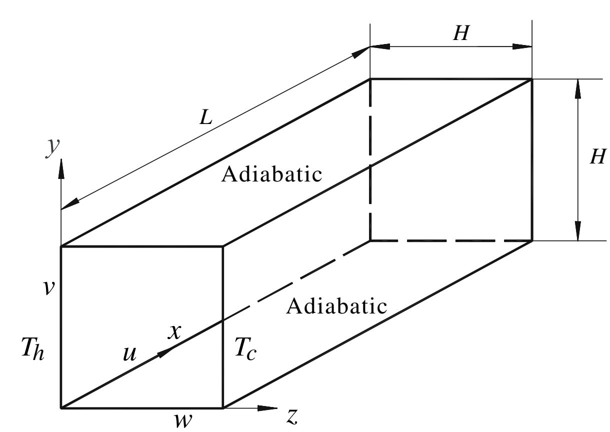

Fig. 1 Flow geometry and coordinate system

x, y and z direction, respectively. The dimensionless temperature $\tilde{\theta}$ is defined as

$$\tilde{\theta} = \frac{T - T_c}{T_h - T_c} \tag{6}$$

And the Reynolds number is defined as

$$Re_\tau = \frac{u_\tau H}{v} \tag{7}$$

where v is the fluid kinematic viscosity. The mean pressure gradient is –4 in the streamwise direction. The fluctuating pressure is given by $p = \hat{p}/(\rho u_\tau^2)$, where $\hat{p}$ is the dimensional fluctuating pressure and ρ is the density. The Grashof number, Gr, is based on the temperature difference between the two vertical walls ΔT and the duct width H. In the present simulation, the maximum Gr of 10^7 has been chosen to meet the requirement of adopting the Boussinesq approximation in small ducts ($H = 0.14$ m) using air as heat transfer medium ($Pr = 0.7$) at 30*degr*C temperature difference. In these conditions, if the reference temperature T_0 is 293 K, this difference in temperature induces maximum variation in density of 9.2%.

No-slip boundary conditions are imposed for the velocity components at the walls, the two vertical walls are assumed to be at the constant but different temperatures, and the horizontal walls are assumed thermally adiabatic. The periodic boundary conditions are adopted in the x-direction for velocities, dimensionless temperature and the fluctuating pressure. And it is these periodic conditions at the domain inlet and outlet that make the fluid flow and heat transfer fully developed, indicating that the velocity and temperature distribution at each cross section is identical in the streamwise direction.

The detailed computational parameters for the present work are given in Table 1. A rectangular region of size $H \times H \times 6.4H$ in the y, z and x-direction, respectively is taken as the computational domain, and the grid system adopted has points of $128 \times 128 \times 256$ (4.1943×10^6) nodes in the three dimensions, respectively. The grid points are positioned in a non-uniform manner by the algebraic stretching technique along the wall-normal direction [16]. Take the direction normal to the bottom wall as an example, the grid in the y-coordinate is determined by

$$y_j = \frac{1}{2}(b-1)\left[\frac{a^{2j/N_y} - 1}{a^{2j/N_y - 1} - 1}\right] \quad j = 0, 1, \ldots, N_y \tag{8}$$

where $a = (b+1)/(b-1)$, N_y is the number of grid points in the y-direction and $b = 1.05$ is the stretching parameter.

Table 1 Computational parameters

Reynolds number Re_τ	400
Grid	$256 \times 128 \times 128$
Computational environment	ShuGuang4000A/Shanghai Supercomputer Center
Computation domains	$6.4H \times H \times H$
Grid spacing	
x-direction	$0.025H$
y, z-direction	0.0015~$0.0127H$
Integrated time period for averaging	$40\ H/u_\tau$
Time increment	$5 \times 10^{-5} H/u_\tau$

3 Numerical method

There are two methods available for DNS studies, i.e., spectral method and finite difference/volume method. Spectral method is known to be capable of providing high resolution solution. Recently, the high order finite difference schemes have been widely used for the DNS studies [19–22]. For the same grid points, high order finite difference scheme can provide high resolution solution for velocity fluctuation which is similar to the resolution provided by the spectral method [23]. Generally speaking, the finite difference scheme can be carried out much easier than the spectral method. In the present DNS study the finite difference method is adopted, and a maximum of seven grids point are used in the evaluation of the convective and viscous derivatives. With a seven-point stencil, the convective and viscous terms are approximated to fifth- and sixth order accuracy, respectively [23]. And MAC type grid is employed to prevent checkerboard pressure fields.

The governing equations are integrated in time using the fractional step method. The Adams–Bashforth scheme is used for time advancement except that the implicit method is adopted for the time advancement of the pressure. The numerical procedures are as follows. A two-step time advancement scheme is implemented starting with the calculation of an intermediate velocity field,

$$\begin{aligned} &\frac{u_i^* - \tilde{u}_i^n}{\Delta t} + \left[\frac{3}{2}\left(\tilde{u}_j \frac{\partial \tilde{u}_i}{\partial x_j}\right)^n - \frac{1}{2}\left(\tilde{u}_j \frac{\partial \tilde{u}_i}{\partial x_j}\right)^{n-1}\right] \\ &= \frac{1}{Re_\tau}\left[\frac{3}{2}\left(\left(\frac{\partial}{\partial x_j}\left(\frac{\partial \tilde{u}_j}{\partial x_j}\right)\right)^n + j_y\left(\frac{Gr\tilde{\theta}}{Re_\tau}\right)^n\right)\right. \\ &\quad \left. - \frac{1}{2}\left(\left(\frac{\partial}{\partial x_j}\left(\frac{\partial \tilde{u}_j}{\partial x_j}\right)\right)^{n-1} + j_y\left(\frac{Gr\tilde{\theta}}{Re_\tau}\right)^{n-1}\right)\right] + 4i_x \end{aligned} \tag{9}$$

where the i_x represents the unit vector in the stream-wise direction and j_y represents the unit vector in the normal wall direction (y-direction) as shown in Fig. 1. The index n symbolizes the current time step, n–1 stands for the previous time-step and * represents the intermediate step. The velocity for next time-step $n + 1$ is related to the intermediate values through

$$\frac{u_i^{n+1} - u_i^*}{\Delta t} = \left(-\frac{\partial p}{\partial x_i}\right)^{n+1} \tag{10}$$

Substituting the new velocity field u_i^{n+1} into the continuity equation, following Poisson equation for pressure can be obtained:

$$\frac{\partial^2 p^{n+1}}{\partial x_i^2} = \frac{1}{\Delta t}\frac{\partial u_i^*}{\partial x_i} \tag{11}$$

By using Adams–Bashforth scheme for time advancement the energy equation can be discretized as:

$$\frac{\tilde{\theta}^{n+1} - \tilde{\theta}^n}{\Delta t} + \left[\frac{3}{2}\left(\tilde{u}_j\frac{\partial\tilde{\theta}}{\partial x_j}\right)^n - \frac{1}{2}\left(\tilde{u}_j\frac{\partial\tilde{\theta}}{\partial x_j}\right)^{n-1}\right]$$
$$= \frac{1}{PrRe_\tau}\left[\frac{3}{2}\left(\frac{\partial}{\partial x_j}\left(\frac{\partial\tilde{\theta}}{\partial x_j}\right)\right)^n - \frac{1}{2}\left(\left(\frac{\partial}{\partial x_j}\left(\frac{\partial\tilde{\theta}}{\partial x_j}\right)\right)^{n-1}\right)\right] \tag{12}$$

Once p^{n+1} is solved from Eq. 11 the velocity field for the next time-step can be evaluated by Eq. 10, then the energy equation can be solved from Eq. 12. Such kind of advancement is executed step by step, until the required solutions are obtained.

4 Code validation and initial fields effect

Because there is no benchmark solution for the fully developed turbulent and heat transfer in the square duct with natural convection at the cross section as presented in this paper, we can only validate our code through comparing the result of $Gr = 0$, that is, the case for which the buoyancy forces is neglected, with available solutions from the previous DNS studies for time-average velocity and temperature field and other turbulence statistics. Two kinds of point-stencil are used for the spatial derivatives of the Poisson equation, Eq. 11, for pressure. That is, the fourth order accurate scheme with a stencil of four grids [23] and second order central difference are used. Because the MPI parallel programming language is used to speed-up the calculations in the present study, super-relaxation method (SOR) to solve Eq. 11 in a parallel manner is suitable. It is well known that fourth order accurate finite difference is expensive for the SOR method because a great deal of data needs to be exchanged between the areas. On the other hand, compared with the fourth order accurate finite difference, second order central difference is most economical and convenient for the data change. Our preliminary computational results show that the second order central difference for the spatial term in the Poisson equation does not affect the accuracy of numerical solution. Thus it is used in this paper in the subsequent computations. Detailed comparisons will be provided in the later discussion. Table 2 gives the computational condition for the example. In the table "2nd order" represents the second order central difference for all spatial derivatives in the governing Eqs. (1)–(5), "higher order" represents the convective and viscous terms being approximated to fifth- and sixth order accuracy, respectively, and fourth order accuracy difference for Poisson equation 11, and "higher order-2p" is similar to the higher order, but the Poisson equation 11 is discretized by second order central difference. In the following comparisons between our numerical predictions and those available in the literatures will be conducted in six aspects for the fully developed fluid flow and heat transfer in a square duct.

Table 2 Computational conditions for example

Case	2nd order	2nd order	Higher order	Higher order-2p
Re_τ	400			
Computational domains	$6.4H \times H \times H$ $(x \times y \times z)$			
Grid number	$128 \times 128 \times 128$	$256 \times 256 \times 256$	$128 \times 128 \times 128$	$128 \times 128 \times 128$
Grid spacing				
x direction x^+	20	10	20	20
y and z direction y^+ and z^+	0.6~5.0	0.21~2.7	0.6~5.0	0.6~5.0
Integrated times for averaging	450 H/u_m			
Time increment	$5 \times 10^{-5} H/u_\tau$			
Computational environment	ShuGuang4000A/Shanghai Supercomputer Center			

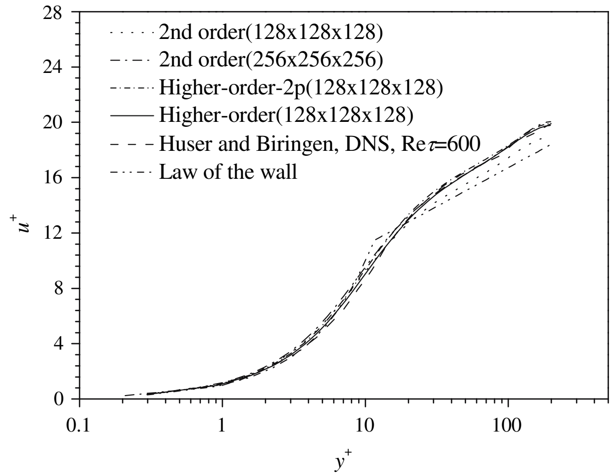

Fig. 2 Comparing mean streamwise velocity along the wall bisector with the law of the wall

The simulated mean steamwise velocity profile along the wall bisector (z = 0.5) is shown in Fig. 2 in wall coordination and compared with the law of wall, which reads

$$\langle u^+ \rangle = 2.5 \ln y^+ + 5.5 \tag{13}$$

where $y^+ = yRe_\tau$. It can be observed that the present mean velocity profile varies linearly with y^+ in the viscous sublayer, agreeing well with $u^+ = y^+$. However, beyond the viscous sublayer the predicted mean velocities are higher than determined by Eq. 13. It can be seen in Fig. 2 that the mean velocities of the 2nd order with finer gird and higher order are agreeable well with the solution of Huser and Bringen [16], while the solution of the second order with coarse gird is less than that of Huser and Biringen but closer to Eq. 13.

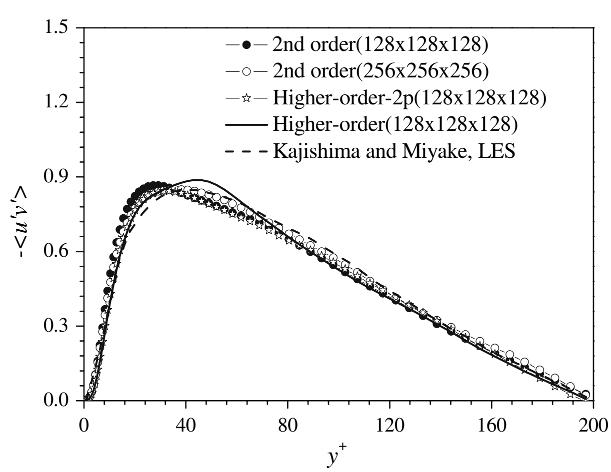

Fig. 3 Comparison of Reynolds stress – $\langle u'v' \rangle$ along the corner bisector

Figure 3 shows that the predicted distribution of Reynolds stress $-\langle u'\ v' \rangle$ along the wall bisector agrees with that reported by Kajishima and Miyake [10]. The ensemble-averaged skin friction variation as function of the distance along the wall is shown in Fig. 4. The results obtained from present simulation are in accordance with the data from Huser and Biringen [16]. It is observed in Fig. 4 that the local maximum value in τ_w is at the wall bisector and the corner.

The rms velocity fluctuations near the wall are shown in Fig. 5. The present results provide excellent agreement with the other data (Kajishima and Miyake [10], Huser and Biringen [16]) in the viscous sub-layer. And in the central region of duct, the result of LES is a bit larger than the present simulation for u_{rms} and is a bit less than the present one for v_{rms} and w_{rms}. It can be seen in Fig. 5 that the results of the two higher order difference methods are closer to the numerical data of [10] and [16] than the second order difference solutions. The differences in rms velocity fluctuations vs. y^+ distributions between our predictions and those of Huser and Biringen's may be attributed to Reynolds number difference.

The predicted mean temperature profile at the wall bisector along the z direction is shown in Fig. 6. The present results are in good agreement with that of Piller and Nobile [1]. As can be expected, the temperature gradient is steeper near the wall than that of the central. Fig. 7 gives the distribution of mean temperature normalized by the Θ_τ, where Θ_τ is defined as

$$\Theta_\tau = \frac{q_w}{\rho c_p u_\tau} \tag{14}$$

where q_w is the heat flux, and c_p is he specific heat. It is observed in Fig. 7 that the $\Theta^+ (= \theta/\Theta_\tau)$ is linear near the wall for $y^+ < 8$, where the distribution of present

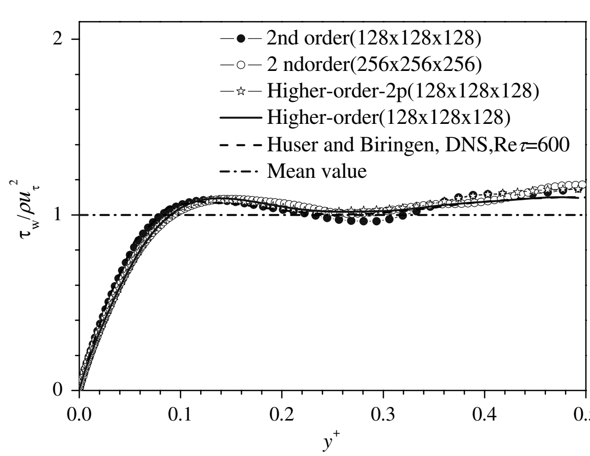

Fig. 4 Comparison of ensemble-averaged wall stress variation

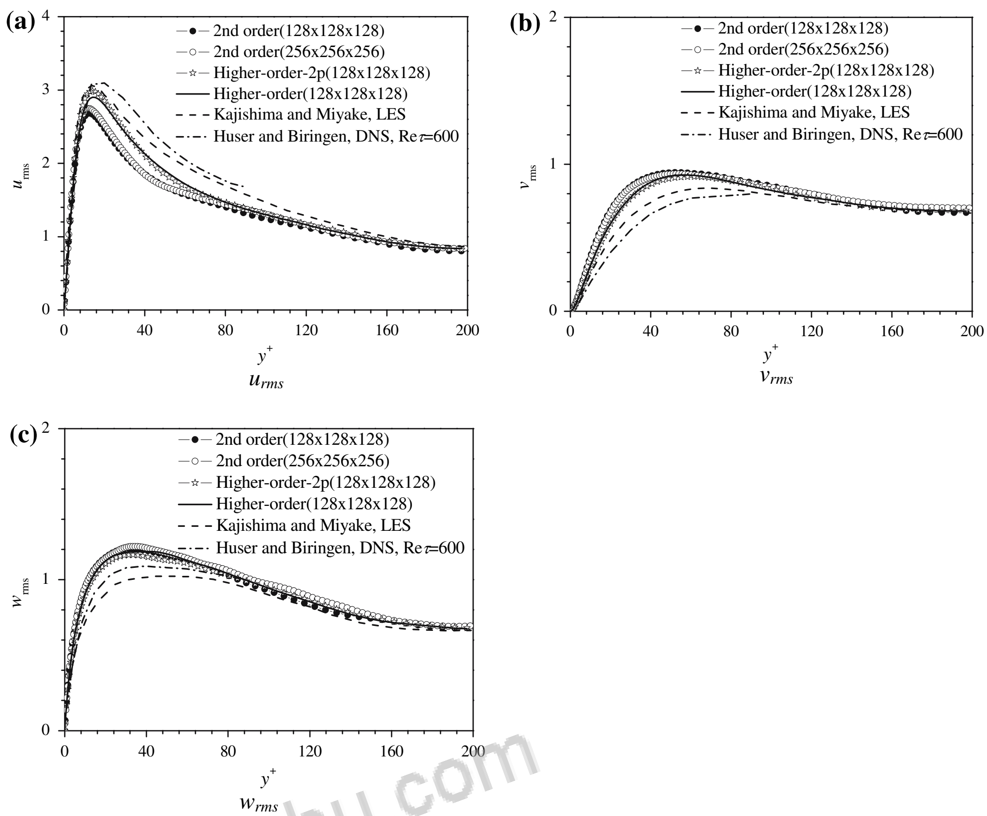

Fig. 5 Comparison of rms fluctuations along the wall bisector normalized by the local friction

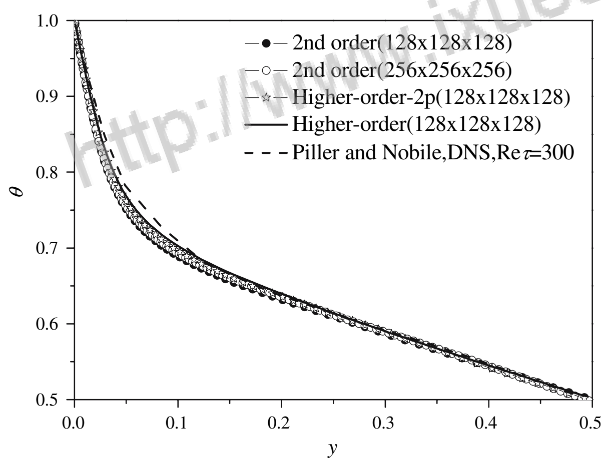

Fig. 6 Comparison of mean temperature profile at the wall bisector along the z direction

simulation provides the excellent agreement with the $\Theta^+ = Pr\ y^+$. And the distributions of the two higher order methods are consistent in the central region of duct, which are slightly higher than that of the solutions of second order difference.

Figure 8 presents the comparison of the local Nusselt number at the hot wall between the present results and that of Piller and Nobile [1]. The Nusselt number is defined as

$$Nu = \frac{q_w H}{\lambda \Delta T} \tag{15}$$

It can be seen from Fig. 8 that the local Nusselt number from the second order difference with coarse grid is larger than the solutions of the two higher order schemes and second order difference with finer grid. The differences between present simulation and that of Piller and Nobile is owing to the different in Reynolds number.

Table 3 presents the comparison of streamwise characteristic velocity, friction coefficient and mean Nusselt number. It can be seen in Table 3 that the mean velocity and the velocity in the central line (that is maximum velocity) from the solution of the second order difference with coarse grid are less than the results of reference [10], while the results of second order difference with finer grid and the two higher order difference methods are quite consistent, and are in accordance with the results of reference [10]. Table 3 gives also the friction coefficient correlation from experimental work [24]. Compared with the correlation, the predicted friction coefficient from the higher order-2p scheme has the least relative deviation.

From the above comprehensive comparisons, it can be concluded that the present DNS simulation is comparable with the solutions available in the litera-

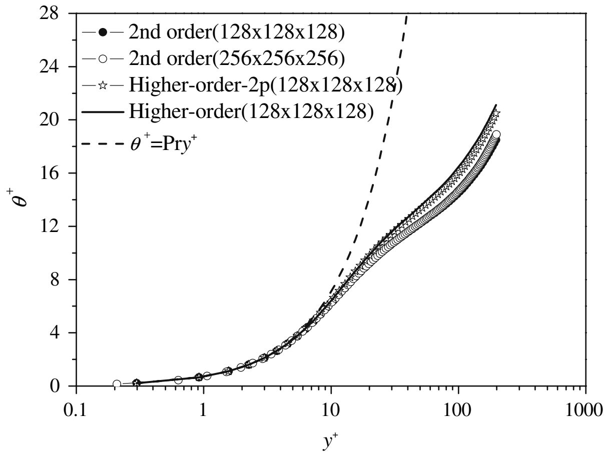

Fig. 7 Comparison of mean temperature profile normalized by Θ_τ

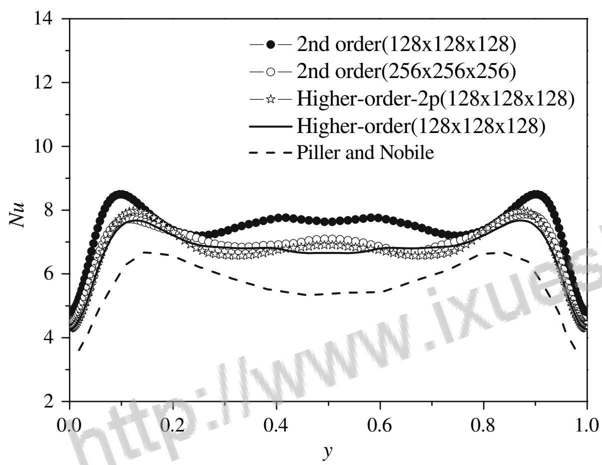

Fig. 8 Comparison of local Nusslet number at the warm wall

ture, and the combination with second order central difference for the pressure Poisson equation and higher order difference for the other terms can result in satisfactory solutions, which is still economical for the MPI parallel programming language environment.

In our numerical simulation, two kinds of initial fields practice are adopted in simulations. In one practice the computational results of lower *Gr* number are used as the initial fields of next higher *Gr* number, in the other practice the solutions for laminar duct flow at the same *Gr* in conjunction with a fluctuation velocity field derived from a random number generator are adopted as the initial ones. The results show that the choice of initial conditions does not influence the final solutions, although it has an influence on the integration time required to reach a statistically stationary state. So the solutions that have been obtained are in fact unique in the present simulation with stable natural convection on the cross section.

5 Results and discussion

Before the presentation of the predicted results, some numerical aspects of our simulation are described.

It should be noted that, theoretically, the ensemble averaged flow and temperature field should have symmetric distributions on the cross section and the contour of which should be smooth. Computationally, the complete symmetry can only be obtained if the flow and temperature are integrated for a long-enough time period and large sample sizes are used for averaging. Otherwise, the results of averaging may be affected by some instantaneous fields, leading to certain asymmetry in the fields. With such understanding in mind, in our numerical practice the discretized equations were integrated for a sufficiently long time period (80 non-dimensional time units) to ensure statistically steady state of the turbulence flow and symmetrical character. The steady state was identified when the mean value of the total kinetic energy approaches a constant. The averaging process was performed both in time and in the streamwise direction because the fully developed flow is obtained, i.e., the velocities and the dimensionless temperature distribution on the cross section is identical in the streamwise direction and the heat transfer is independent on the inlet temperature. The mean velocities were obtained by averaging for the 40

Table 3 Comparison of streamwise characteristic velocity, friction coefficient and mean Nusselt number for the example

Case	2nd order	2nd order	Higher order-2p	Higher order	reference [10]
Grid number	128^3	256^3	128^3	128^3	–
u_c	18.94	20.04	19.90	19.77	20.0
u_{mean}	14.59	15.24	15.50	15.35	15.5
Re_{m}	5838	6096	6199	6138	6200
$C_{f,cal}$	9.39×10^{-3}	8.61×10^{-3}	8.32×10^{-3}	8.64×10^{-3}	–
$C_{f,\exp} = 0.073\ Re^{-0.25}$[24]	8.38×10^{-3}	8.26×10^{-3}	8.23×10^{-3}	8.24×10^{-3}	8.23×10^{-3}
Relative deviation of friction coefficient,ε	12%	4.2%	1.2%	2.9%	–
Mean Nusselt number, *Nu*	7.48	7.11	6.81	6.77	–

non-dimensionless time units, as shown in Table 1. This averaged time period corresponds to the time that a fluid particle would take which is at the duct centerline and travels through a distance equal to about 800 H. This distance is much longer than the entrance length which is about 80 H [16]. In order to calculate the fluctuating component of velocity (u', v' w') at any time, the obtained ensemble mean velocity ($\langle u\rangle$, $\langle v\rangle$, $\langle w\rangle$) were subtracted from the resolved instantaneous velocity at each node. These fluctuating components of the velocity field were then uses to calculate the different statistics of the turbulent field at that time instant. For example, they were averaged in time and space to obtain the ensemble average ($\langle u'\ u'\rangle$, $\langle u'\ v'\rangle$, etc.). Owing to the explicit treatment of the advection term, the CFL number must be less than a certain value. The time step Δt was restricted to a value satisfying following condition [15]

$$\mathrm{CFL}_{\max} = \Delta t_{\max}\left[\frac{|u|}{\Delta x}+\frac{|v|}{\Delta y}+\frac{|w|}{\Delta z}\right] \le 0.3 \tag{16}$$

which resulted in the choice $\Delta t = 5 \times 10^{-5} H/u_\tau$. The MPI parallel programming language was used to speed-up the calculations. Maximal CPU number is up to eight in the DNS, obtaining satisfactory performances.

In the following simulated results will be presented in the aspects of mean flow and temperature, spatial Reynolds stress, streamwise momentum equation budget and energy budget.

5.1 Mean flow and temperature characteristics

The mean secondary and streamwise velocity distributions at different Grashof numbers are presented in Fig. 9, where the contours represent the steamwise velocity component and the vector fields represent the cross-stream vector. All velocities shown there are normalized by friction velocity and the distances are normalized with the duct width. In the figure both the contours of the mean steamwise velocity and the secondary velocity vectors in the cross section are shown. Figure 9a shows the secondary flow velocity vectors at $Gr = 0$. It can be observed that in each corner there are two streamwise and counter-rotating vortices that are symmetrical about the corner bisector. In the present simulation $Re_\tau = 400$, the vortex centers are close to the corner and the secondary flows are quite weak near the wall bisector, and such numerical findings are consistent with the results in literature [16]. The vortices have no visible change in the vector field for $Gr = 10^4$, see Fig. 9b, indicating that for $Gr \le 10^4$ the transport process at the cross section is dominated by diffusion. However, with the further increase in Grashof number, the vortices of secondary flow are changed by buoyancy body force. It can be clearly observed that the symmetry of two streamwise and counter-rotating vortices is destroyed at $Gr = 10^5$. The vortex near the vertical wall at the down left quadrant of the duct cross section is larger than that near the horizontal wall, see Fig. 9c. For the case of $Gr = 10^6$ a large vortex dominants the flow in the centre of the cross section, and the streamline contour shapes change from approximately square to rhombus-like. Only one small vortex can be observed in each corner, which exists near the horizontal wall at the down left quadrant (Fig. 9d). When Gr is up to 10^7, the flow field on the cross section is dominants by only one large vortex, and the streamline contour shape like slightly-tilted horizontal rectangles. And there exists an updraft near the hot wall. The cross-section flow in the centre region is weaker than that near the surrounding walls along which boundary layer flow occurs.

Here, the reason why the vortices pattern of cross-stream is changed with the increase of Gr number is discussed. We consider now the balance of forces which contribute to the generation of cross flow. The Reynolds-averaged equations for the cross flow are presented by

$$\langle v\rangle\frac{\partial\langle v\rangle}{\partial y}+\langle w\rangle\frac{\partial\langle v\rangle}{\partial z} = -\frac{\partial\langle p\rangle}{\partial y}+\frac{1}{Re_\tau}\left(\frac{\partial^2\langle v\rangle}{\partial y^2}+\frac{\partial^2\langle v\rangle}{\partial z^2}\right) -\frac{\partial\langle v'v'\rangle}{\partial y}-\frac{\partial\langle v'w'\rangle}{\partial z}+\frac{Gr}{Re_\tau^2}\theta \tag{17}$$

$$\langle v\rangle\frac{\partial\langle w\rangle}{\partial y}+\langle w\rangle\frac{\partial\langle w\rangle}{\partial z} = -\frac{\partial\langle p\rangle}{\partial z}+\frac{1}{Re_\tau}\left(\frac{\partial^2\langle w\rangle}{\partial y^2}+\frac{\partial^2\langle w\rangle}{\partial z^2}\right) -\frac{\partial\langle v'w'\rangle}{\partial y}-\frac{\partial\langle w'w'\rangle}{\partial z} \tag{18}$$

Equations 17 and 18 show that the turbulence stress gradient vector, D_R, can be presented as $\left(-\frac{\partial\langle v'w'\rangle}{\partial y}-\frac{\partial\langle w'w'\rangle}{\partial z}, -\frac{\partial\langle v'v'\rangle}{\partial y}-\frac{\partial\langle v'w'\rangle}{\partial z}\right)$ in y–z plane, pressure gradient (D_P) and thermal buoyancy force (D_T) vectors can be wrote as $\left(-\frac{\partial\langle p\rangle}{\partial z}, -\frac{\partial\langle p\rangle}{\partial y}\right)$ and $\left(0, \frac{Gr}{Re_\tau^2}\theta\right)$, respectively, Figs. 10 and 11 show the distributions of D_R, D_P, $D_\mathrm{R} + D_\mathrm{P}$ and $D_\mathrm{R} + D_\mathrm{P} + D_\mathrm{T}$ at the cases of $Gr = 10^4$ and 10^7, respectively. It is observed from Fig. 10 that the gradient of turbulence stress seems to be the major driving force of the flow toward corner (see Fig. 10a), whose direction is opposite to that of pressure gradient. The pressure profiles have the gradient along the wall, and the imbalance between the

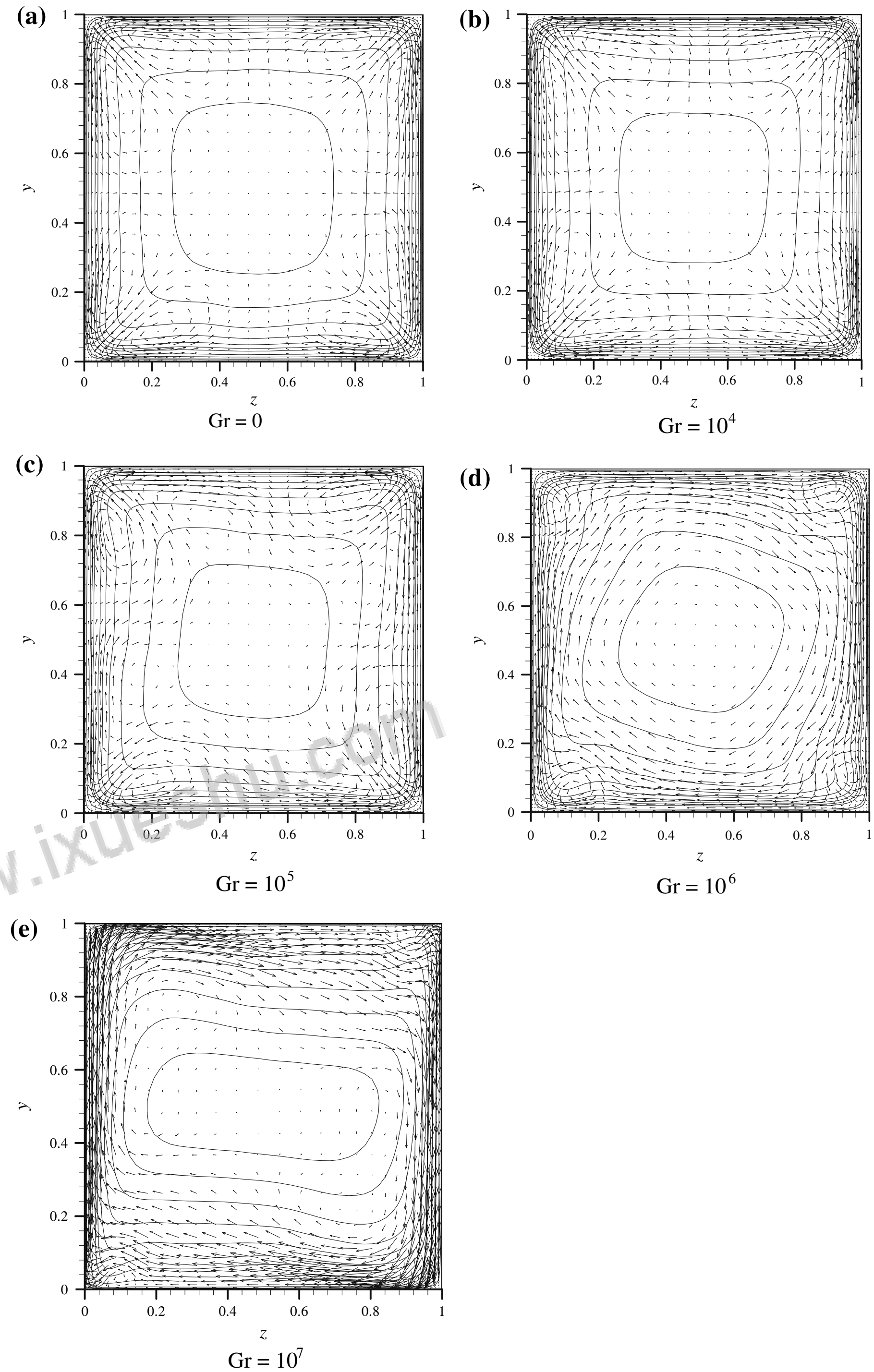

Fig. 9 Mean secondary and streamwise velocity distribution at various Grashof number; **a** $Gr = 0$; **b** $Gr = 10^4$; **c** $Gr = 10^5$; **d** $Gr = 10^6$; **e** $Gr = 10^7$

gradient of the turbulence stress field and that of the corresponding pressure field near wall, which is shown in Fig. 10c, is the origin of the secondary vortices, because the distribution of DR + DP is agreeable well with Fig. 9a at the corner. The result is consistent with that of Kajishima and Miyake [10] for the case of $Gr = 10^4$. And it can be seen from Fig. 10d that distribution of $D_R + D_P + D_T$ is well in accordance with that of $D_R + D_P$, which show that the thermal buoyancy force is very small at $Gr = 10^4$, as shown in Fig. 12a. The contour presents the distribution of temperature that will be discussed in the following section. The thermal buoyancy force can be neglect compared with the terms of turbulence stress gradient and pressure. So the turbulence stresses have an important effect on the generation of secondary flow at

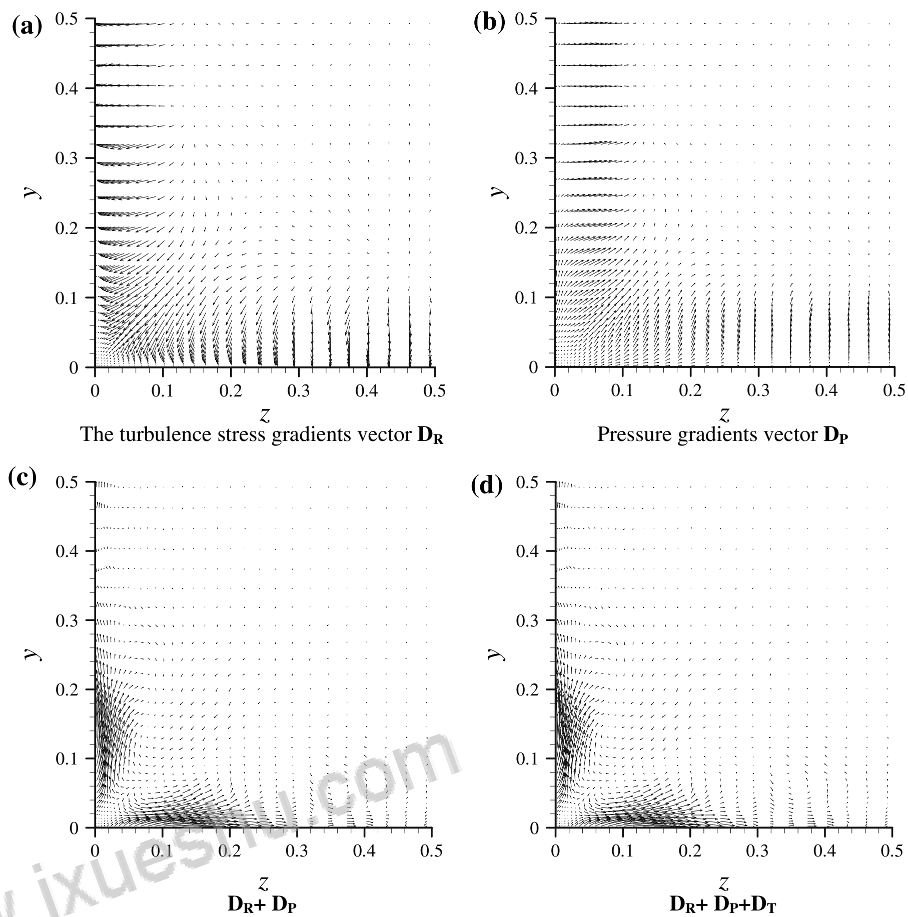

Fig. 10 The distributions of turbulence stresses gradient D_R, pressure gradient D_P, $D_R + D_P$ and $D_R + D_P + D_T$ (D_T represents thermal buoyancy force) at $Gr = 10^4$. **a** The turbulence stress gradients vector $\mathbf{D_R}$. **b** Pressure gradients vector $\mathbf{D_P}$. **c** $\mathbf{D_R + D_P}$. **d** $\mathbf{D_R + D_P + D_T}$

low *Gr* number. But with the increase of *Gr* number, it can be seen from Fig. 11 that the thermal buoyancy force is important on the cross-stream. The distribution of turbulence stress gradient vector at $Gr = 10^7$ is the same as $Gr = 10^4$ (see Fig. 11a). Figure 11c shows that the distribution of $D_R + D_P$ is almost agreeable with that of D_P on the cross section except the regions near the down-left corner, indicating that the contribution of pressure gradient (see Fig. 11b) increases obviously compared with turbulence stress gradient, and the distribution of $D_R + D_P + D_T$ (see Fig. 11d) reflects the cross-stream pattern, as shown in Fig. 9e, but the turbulence stress will weaken the effect of the thermal buoyancy force near the down-left corner. Figure 11 shows that the thermal buoyancy force is the main reason why the cross-stream pattern is changed with the increase of *Gr* number, and it is somewhat decreased owing to the turbulence stress. It can be seen from Fig. 12 that the thermal buoyancy force greatly increases at $Gr = 10^7$ compared with $Gr = 10^4$.

It is observed from the mean steamwise velocity contour at $Gr = 0$ in Fig. 9a that the isotachs are bent toward the corner, indicating an appreciable increase in $\langle u \rangle$ in the corner region. With the increase of *Gr*, the bulging of the steamwise velocity contours toward the corners is more and more stronger. For $Gr = 0$, the local maximum for $\langle u \rangle$ exists at the wall bisector, the occurrence of a local $\langle u \rangle$ maximum at the wall bisector is a low-Reynolds number effect [16]. However, the local maximum position for $\langle u \rangle$ is displaced from the wall bisector to the lower end of the hot wall and contrary for the cold wall. Figure 13 plots the ensemble-averaged skin friction variation as a function of the distance along the wall. It is observed that the local maximum value in $\langle u \rangle$ also yields a maximum in τ_w for all *Gr*. The distribution of $\tau_w/(\rho\, u_\tau^2)$ obtained from the present simulations is agreeable with the data from Gavrilakis [15] and Huser and Biringen [16] for $Gr = 0$, see Fig. 4. The maximum value of τ_w increases with the increase of *Gr*. And it is observed also from Fig. 13 that the gradient of $\tau_w/(\rho\, u_\tau^2)$ with respect to *y* towards the corner is steeper for the higher Grashof number near the lower end of hot wall.

Figure 14 shows the mean temperature distribution in the cross section at various Grashof number. For the case of $Gr = 0$ the isotherm lines are parallel to the

Fig. 11 The distributions of turbulence stresses gradient D_R, pressure gradient D_P, $D_R + D_P$ and $D_R + D_P + D_T$ (D_T represents thermal buoyancy force) at $Gr = 10^7$. **a** The turbulence stress gradients vector $\mathbf{D_R}$. **b** Pressure gradients vector $\mathbf{D_P}$. **c** $\mathbf{D_R} + \mathbf{D_P}$; **d** $\mathbf{D_R} + \mathbf{D_P} + \mathbf{D_T}$

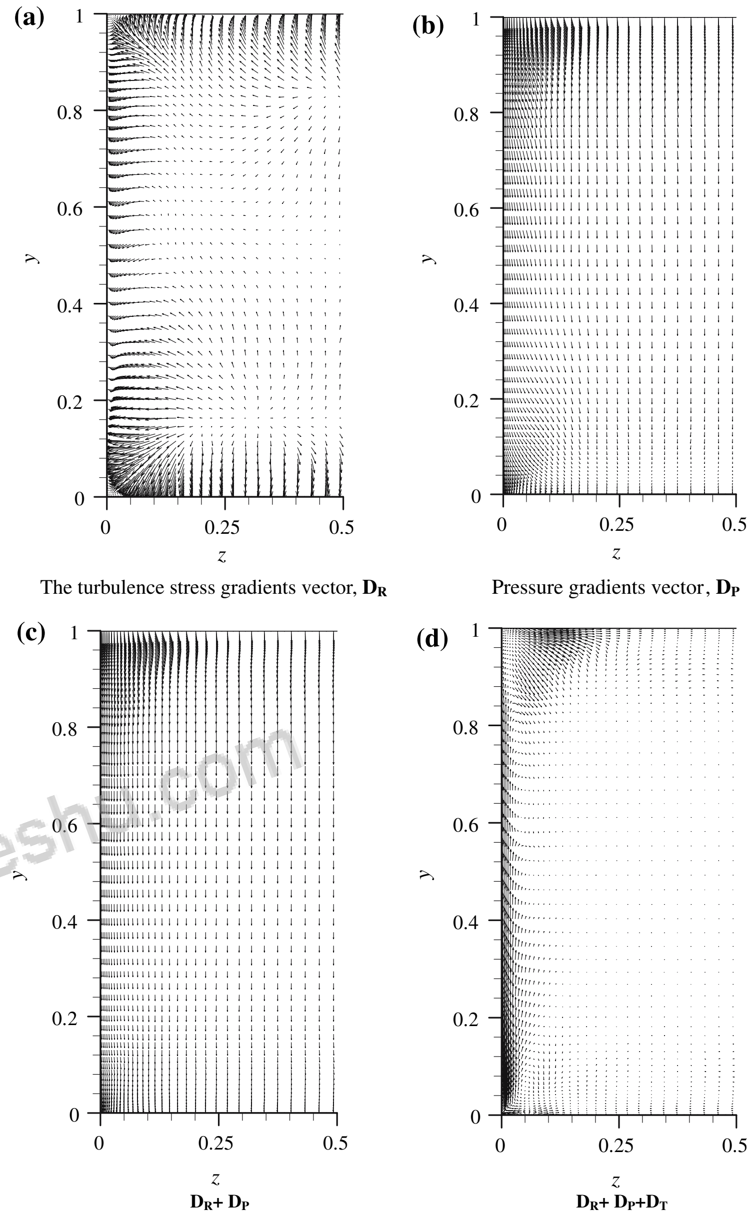

vertical walls except the corner region where each line is bent towards the center direction, indicating an appreciable increase in the mean temperature in the corner near the hot wall and decrease in the corner near the cold wall. With the increase in *Gr*, the global position of the isotherms in the center part of the enclosure gradually changes from vertical to horizontal. And when *Gr* is up to 10^7 the isotherms in the center region of cross section are almost horizontal and parallel to each other. Comparison of local Nusselt number at the hot wall at various Grashof number is given in Fig. 15. It is observed that when *Gr* is less than 10^5 the difference of local Nusselt numbers along the hot wall at different *Gr* is small and their distributions are more and less uniform in the major central part of the wall, however, the difference becomes larger for $Gr = 10^6$ and 10^7. And the local Nusselt number along the hot wall decreases with the increase in *y* except very near the lower corner where there is a sharp increase in a short distance.

Table 4 gives the comparison of the mean Nusselt number at the hot wall at the various *Gr* for $Re_\tau = 400$. Following features may be noted from Table 2. First the mean Nusselt number of the turbulent flow is almost constant when *Gr* number is less than 10^5. Second, the Nusselt number of the laminar flow is less than that of turbulent flow when *Gr* number is less than 10^6. Third, for $Gr = 10^7$ the Nusselt number of the laminar flow is appreciably larger than that of the turbulent flow. Such variation trend can be under-

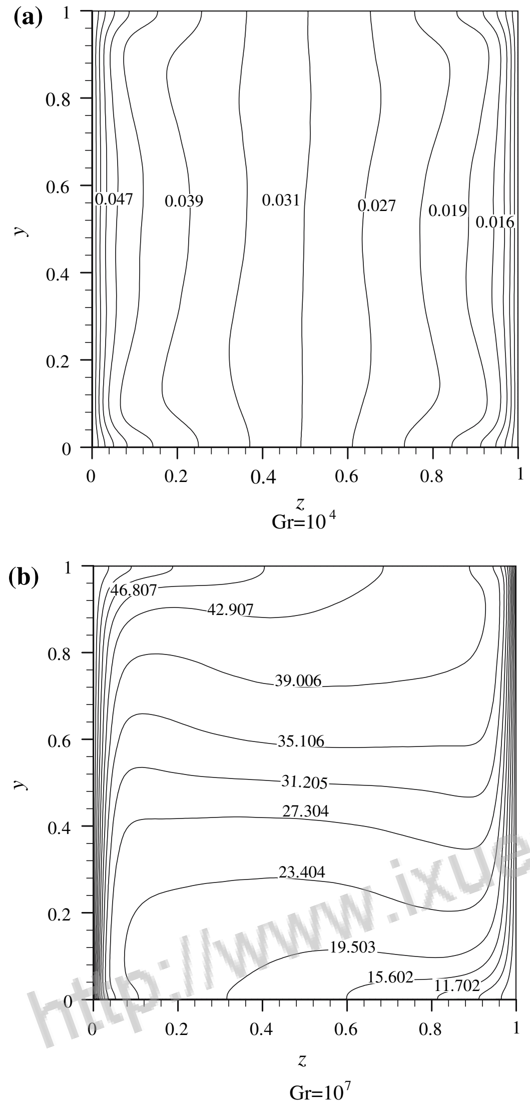

Fig. 12 The contours of thermal buoyancy force at different Grashof number **a** $Gr = 10^4$; **b** $Gr = 10^7$

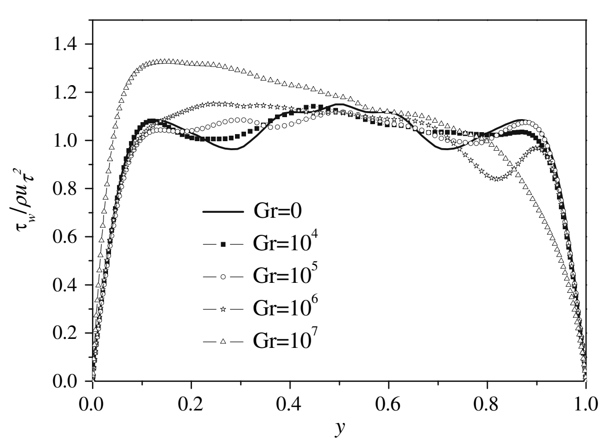

Fig. 13 Comparison of ensemble-averaged wall stress variation with Grashof- number along y direction at the hot wall

stood as follows. In the laminar flow, the flow is controlled by natural convection in the cross section, so mean Nusselt number is increase with the increase of *Gr* number. However, for the turbulent flow, the flow is dominated by the interaction between buoyancy body force and Reynolds stresses due to the turbulent motion and the anisotropy of the normal component of turbulence stress in the cross section. When *Gr* number is less than 10^5 the Reynolds stresses are stronger than the buoyancy force, so the flow state represents basically the secondary flow characteristics. But it is contrary for the higher *Gr* number cases, and due to the negative effect of the Reynolds stresses, the mean Nusselt number decreases with the increase of *Gr* compared with that of laminar flow of the same *Gr* number.

In order to analyze the effect of Reynolds stresses on the Nusselt number, Fig. 16 shows the comparison of local Nusselt number at the hot wall between the laminar and turbulent flow at various Grashof number. It is observed that within the Grashof number studied the local Nusselt number of the laminar flow is basically decreased along y direction, and its values are well below that of the turbulent flow for $Gr \leq 10^5$ because of the secondary flow effect. For the turbulent flow the maximum Nusselt number exists near the corner while the local Nusselt number distribution is more or less uniform when *Gr* is less than 10^5. However, with increase in *Gr*, the increase in *Nu* of turbulent flow is not so fast as that of the laminar flow and when *Gr* number is up to 10^7, the local Nusselt number of the turbulent flow is less than that of laminar flow where coordinate value y is less 0.6 and they are almost equally between 0.6 and 1.0, as shown in Fig. 16d. This variation characteristics show that the natural convection is subject to suppressing by the Reynolds stresses with the increase in *Gr*.

5.2 Reynolds stress' spatial distributions

The Reynolds stress components in the square duct can be analyzed by examining the generation term (M_{ij}^*) in the turbulent stresses transport equation. Generation terms include the mean shear (P_{ij}^*) and buoyancy force production (T_{ij}^*), as shown in Eq. 19. These terms presented in Eqs. 20 and 21 are scaled with bulk velocity

$$M_{ij}^* = P_{ij}^* + T_{ij}^* \tag{19}$$

$$P_{ij}^* = -\left[\left\langle u_i' u_j' \right\rangle^* \frac{\partial u_j^*}{\partial x_k} + \left\langle u_j' u_k' \right\rangle^* \frac{\partial u_i^*}{\partial x_k}\right] \tag{20}$$

Fig. 14 Mean temperature distribution on the cross section at various Grashof-number; **a** $Gr = 0$; **b** $Gr = 10^4$; **c** $Gr = 10^5$; **d** $Gr = 10^6$; **e** $Gr = 10^7$

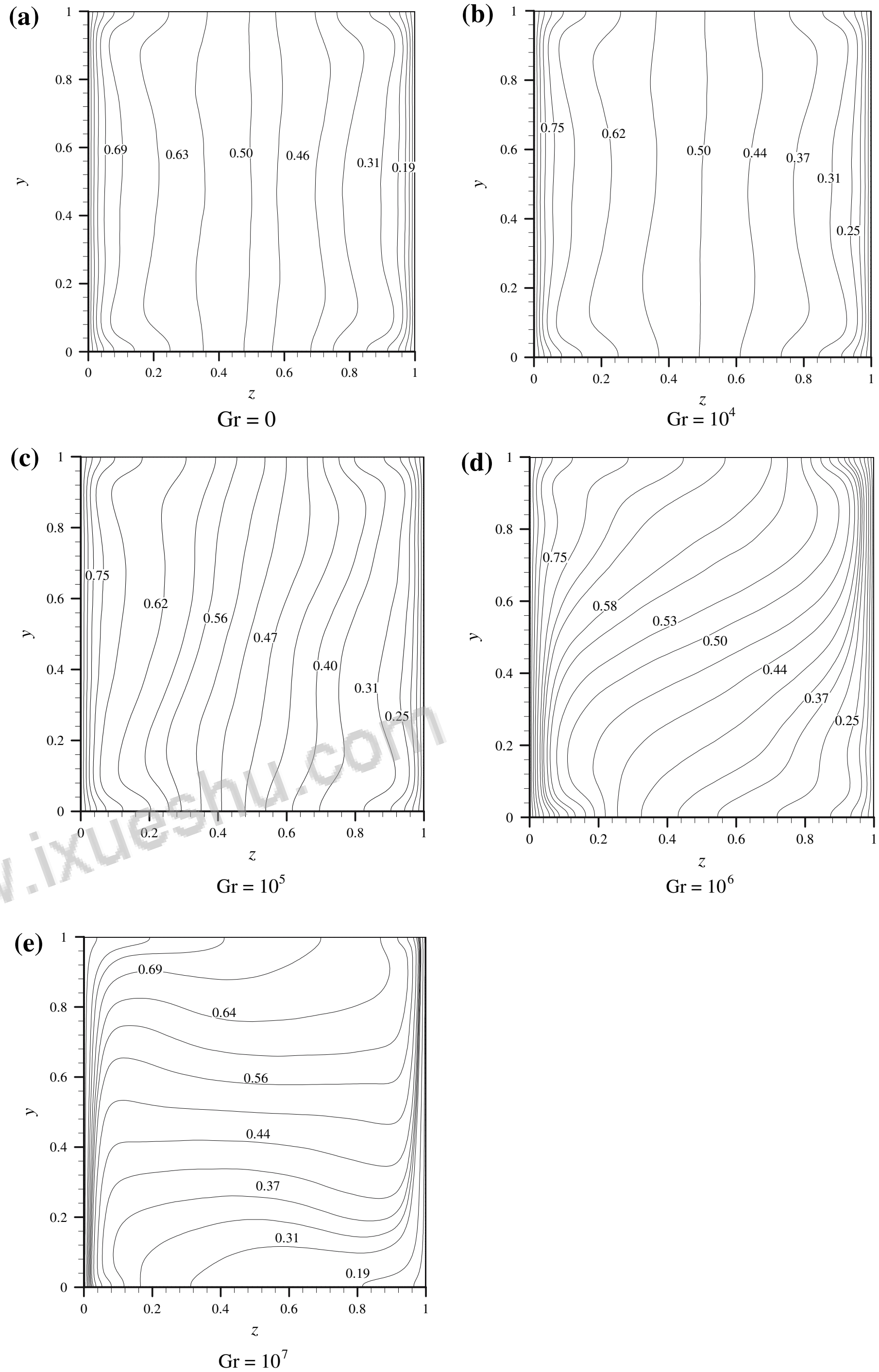

$$T^*_{ij} = -\left[\frac{Gr_i}{Re^2_\tau}\left\langle u'_j\theta'\right\rangle^* + \frac{Gr_j}{Re^2_\tau}\left\langle u'_i\theta'\right\rangle^*\right] \tag{21}$$

where $P^*_{i,j}$ represents the production of the Reynolds stresses from the mean flow, which is result from mean flow velocity gradient together with the Reynolds stresses. It is the main contribution for the production of Reynolds stresses. The T^*_{ij} term represents the production of the Reynolds stresses from the buoyancy, which has important contribution at the high value of *Gr*. The terms of P^*_{ij} and T^*_{ij} are given in the following for the full developed square duct flow. The terms underlined appearing in Eqs. 22 and 23 represent the dominants terms in the different components of P^*_{ij} and T^*_{ij} for the low value of *Gr*.

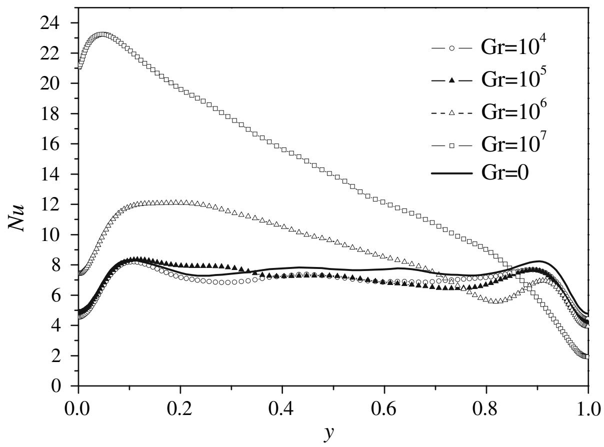

Fig. 15 Comparison of local Nusselt number at the hot wall at various Grashof number

Table 4 Comparison of mean Nusselt number at the hot wall with various Grashof number for Re_τ = 400

Grashof number (Gr)	Laminar flow (Nu)	Turbulent flow (Nu)
0	–	6.81
10^4	2.01	7.01
10^5	4.10	7.10
10^6	8.13	9.00
10^7	15.77	13.90

$$T^*_{ij} = \begin{pmatrix} 0 & -Gr/Re_\tau^2\langle u'\theta'\rangle & 0 \\ - & -2Gr/Re_\tau^2\langle v'\theta'\rangle & 0 \\ - & - & 0 \end{pmatrix} \tag{23}$$

A simplified picture of the complex relationships between the Reynolds stress components through the generation terms 22 and 23 is presented in Fig. 17. It can be seen from the figure that the values of $\langle u'\ u'\rangle^*$, $\langle u'\ v'\rangle^*$ and $\langle u'\ w'\rangle^*$ components depend on the generation P^*_{11}, P^*_{12} and P^*_{13}, respectively, owing to the contribution of the main strain velocity gradient $\partial u^*/\partial y$ and $\partial u^*/\partial z$. The distributions of $\langle v'\ v'\rangle^*$ and $\langle w'\ w'\rangle^*$ are more influenced by the velocity pressure-gradient term, which act as the source term for them. The role of the pressure-strain interaction in the transport equations for the normal Reynolds stresses is associated with a redistribution of turbulent energy among the normal stresses, transferring energy from $\langle u'\ u'\rangle^*$ to the other normal components, $\langle v'\ v'\rangle^*$ and $\langle w'\ w'\rangle^*$ [25]. Figure 17 shows also that $\langle v'\ v'\rangle^*$ and $\langle u'\ v'\rangle^*$ are influenced by $T_{22}(2Gr/Re_\tau^2\langle v'\theta'\rangle)$ and $T_{12}(Gr/Re_\tau^2\langle u'\theta'\rangle$ at the highest Gr number considered, respectively.

Figures 18 and 19 show the cross-stream spatial distribution of the averaged normal and shear Reynolds stresses at Gr = 0, 10^4, 10^6, and Gr = 10^7, respectively. The Reynolds stresses shown in these figures have been scaled with the bulk velocity

$$\left\langle u'_i u'_j\right\rangle^* = 100\left\langle u'_i u'_j\right\rangle / U_b^2 \tag{24}$$

where U_b is the average velocity on the cross section. This scaling has been used to take into account the variability of the average streamwise velocity at different values of Gr number [25]. Contours of the Reynolds stresses at Gr = 0 and Gr = 0.6 (continuous lines) are plotted together with ones corresponding to Gr = 10^4 and 10^7 (discontinuous lines).

Figure 18 shows that the contribution of T^*_{ij} is small at the low Gr number. Slightly changes appear in the contours of the Reynolds stress, but with increase of Gr number, the distribution of Reynolds stresses is changed obviously. The peak value of the primary normal stress $\langle u'\ u'\rangle^*$ for Gr number less than 10^4 (see Fig 18(a)) appears near the wall. Considering the vertical wall, the maximum value of $\langle u'\ u'\rangle^*$ is at z = 0.4 and z = 0.6, which is consistent with the study of DNS in reference [16]. The contour lines are bent toward the

$$P^*_{ij} = \begin{pmatrix} -2\left(\langle u'v'\rangle^*\dfrac{\partial u^*}{\partial y} + \langle u'w'\rangle^*\dfrac{\partial u^*}{\partial z}\right) & -\left(\langle u'v'\rangle^*\dfrac{\partial v^*}{\partial y} + \langle u'w'\rangle^*\dfrac{\partial v^*}{\partial z} + \langle v'v'\rangle^*\dfrac{\partial u^*}{\partial y} + \langle v'w'\rangle^*\dfrac{\partial u^*}{\partial z}\right) & -\left(\langle u'v'\rangle^*\dfrac{\partial w^*}{\partial y} + \langle u'w'\rangle^*\dfrac{\partial w^*}{\partial z} + \langle v'w'\rangle^*\dfrac{\partial u^*}{\partial y} + \langle w'w'\rangle^*\dfrac{\partial u^*}{\partial z}\right) \\ - & -2\left(\langle v'v'\rangle^*\dfrac{\partial v^*}{\partial y} + \langle v'w'\rangle^*\dfrac{\partial v^*}{\partial z}\right) & -2\left(\langle v'v'\rangle^*\dfrac{\partial w^*}{\partial y} + \langle w'w'\rangle^*\dfrac{\partial v^*}{\partial z}\right) \\ - & - & -2\left(\langle v'w'\rangle^*\dfrac{\partial w^*}{\partial y} + \langle w'w'\rangle^*\dfrac{\partial w^*}{\partial z}\right) \end{pmatrix} \tag{22}$$

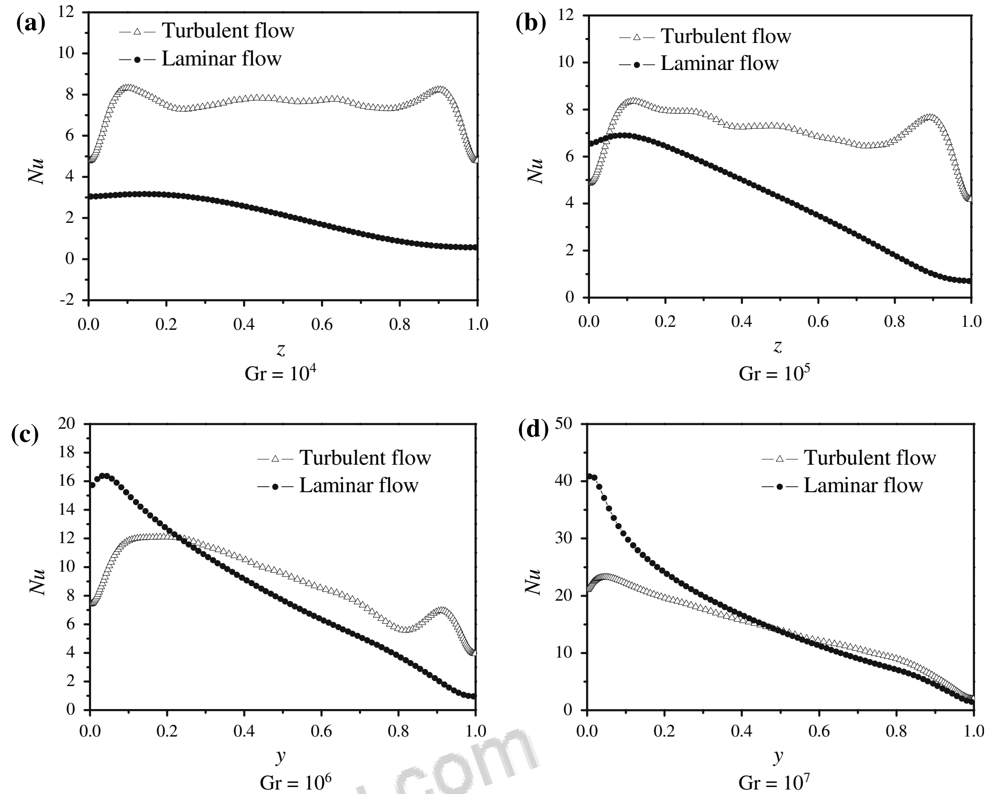

Fig. 16 Comparison of local Nusselt number at the warm between the laminar and turbulent flow wall with various Grashof number; **a** $Gr = 10^4$; **b** $Gr = 10^5$; **c** $Gr = 10^6$; **d** $Gr = 10^7$

center of the duct indicating an appreciable increase for $\langle u'\ u'\rangle^*$ at $Gr = 10^4$. The distribution of $\langle u'\ u'\rangle^*$ disappears symmetric behavior about the wall bisector with increase of *Gr* number. The maximum point of $\langle u'\ u'\rangle^*$ is removed upwards near the hot wall, (Fig 19(a)) and the situation is contrary at the cold wall. For $Gr = 10^7$, the maximum point of $\langle u'\ u'\rangle^*$ is located near the horizontal wall in the region of down-left corner.

The normal stress, $\langle v'\ v'\rangle^*$, attains maximum value near the vertical wall, where high value of the corresponding vertical pressure-gradient terms occurs for the lower *Gr* number. Because the energy transfer from $\langle u'\ u'\rangle^*$ to $\langle v'\ v'\rangle^*$ near the horizontal wall is inhibited by the damping effect of the wall, where the values of $\langle v'\ v'\rangle^*$ are less than that of vertical wall. At higher *Gr* number, the maximum value of $\langle v'\ v'\rangle^*$ is no

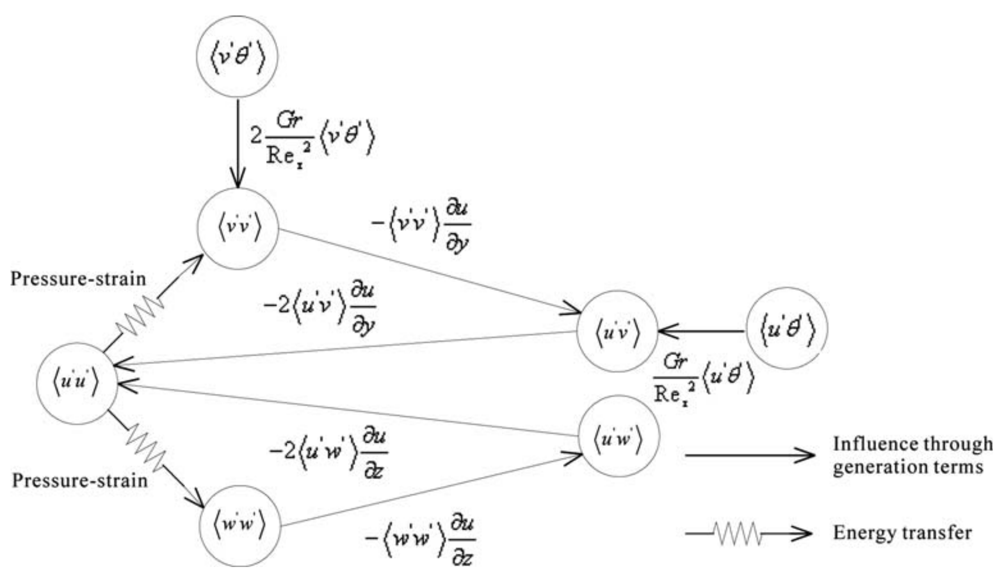

Fig. 17 Main relationships between the Reynolds stresses components through the generation terms M_{ij}

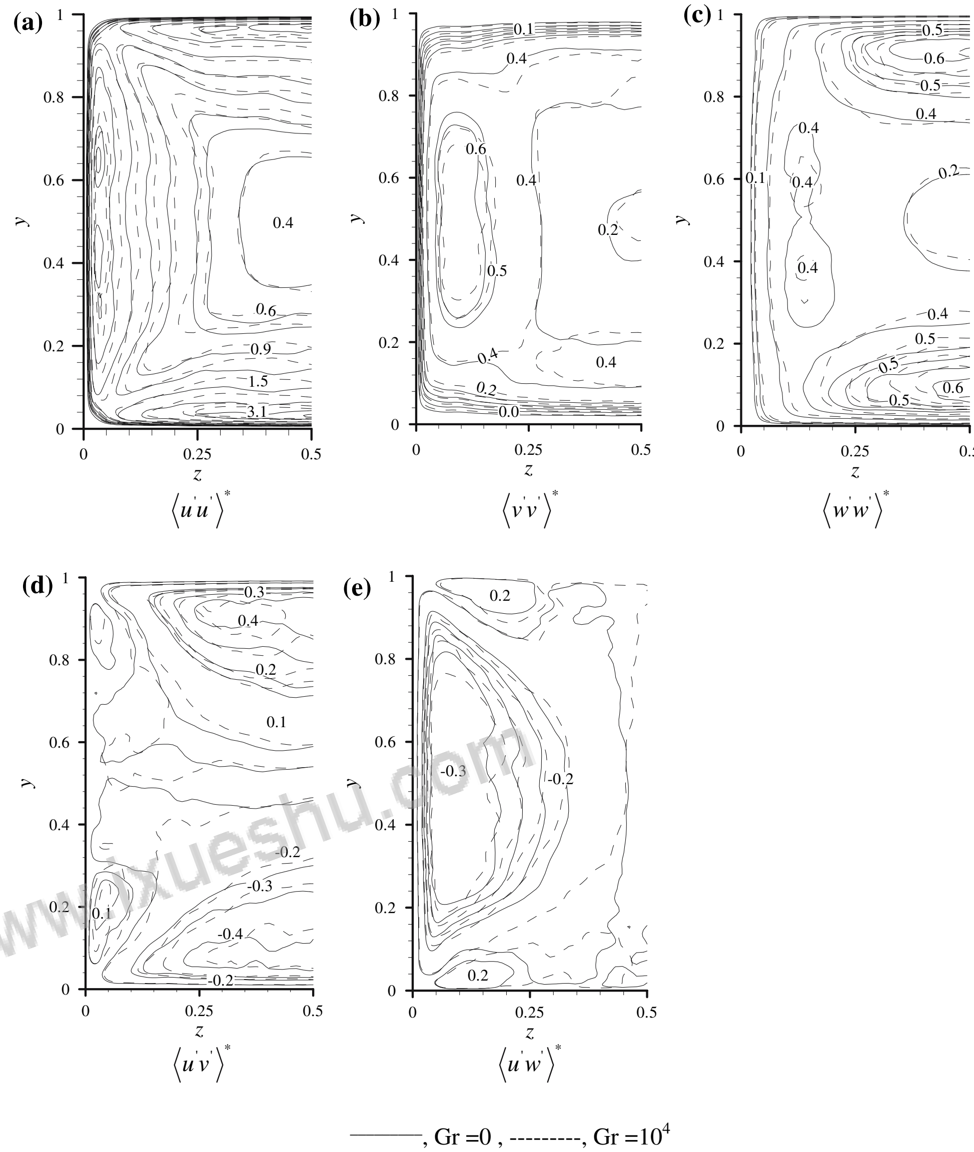

Fig. 18 spatial distributions of Reynolds stress components in square duct flow at $Re_\tau = 400$ for $Gr = 0$ (continuous lines) and $Gr = 10^4$ (discontinuous lines); **a** $< u'u' >^*$, **b** $< v'v' >^*$, **c** $< w'w' >^*$, **d** $< u'v' >^*$, **e** $< u'w' >^*$

longer near the vertical wall, but is at the horizontal wall close to the down-left corner, where the thermally-generated secondary currents occur, as seen in Fig 9(d) and (e). $\langle v' \ v' \rangle^*$ is influenced by $\langle v' \ \theta' \rangle^*$ at higher Gr number, whose magnitude of buoyancy force production term is $2Gr/Re_\tau^2 \langle v'\theta' \rangle^*$. The maximum value of the normal stress $\langle v' \ v' \rangle^*$ is increased by the effect on buoyancy force. The distribution of Reynolds stress $\langle w' \ w' \rangle^*$ is obtained by a 90° rotation of $\langle v' \ v' \rangle^*$ distribution because of flow field symmetry for lower Gr number. But the symmetric behavior of flow field disappears with the increase of Gr, along the horizontal wall bisector the $\langle w' \ w' \rangle^*$ increases where the horizontal advection occurs and decreases along the vertical wall bisector because thermally-generated ascending current occurs.

Figures 18d and 19d show the distribution of Reynolds stress $\langle u' \ v' \rangle^*$, which is mainly affected by the term $-\langle v'v' \rangle^* \partial u^* / \partial y$ in production term P_{12}^* and $T_{12}^*(Gr/Re_\tau^2 \langle u'\theta' \rangle)$ at high Gr number. It should be noted that the region where $\langle u' \ v' \rangle^*$ is positive/negative is corresponding to the region where main velocity gradient $\partial u^*/\partial y$ is negative/positive. It can be seen from Fig. 18d that the value of $\langle u' \ v' \rangle^*$ reduces at the wall bisector ($z = 0.5$) compared to its value at $z = 0.4$. The Reynolds stress $\langle u' \ v' \rangle^*$ increases and reaches a maximum value near the vertical wall for $0.03 < y < 0.3$ when this is approached horizontally from $z = 0.5$, which is consistent with reference [16]. Because $\langle u' \ v' \rangle^*$ is influenced by T_{12}^* at higher Gr number, the $\langle u' \ v' \rangle^*$ distribution is changed obviously at $Gr = 10^7$. The region where the value of $\langle u' \ v' \rangle^*$ is less

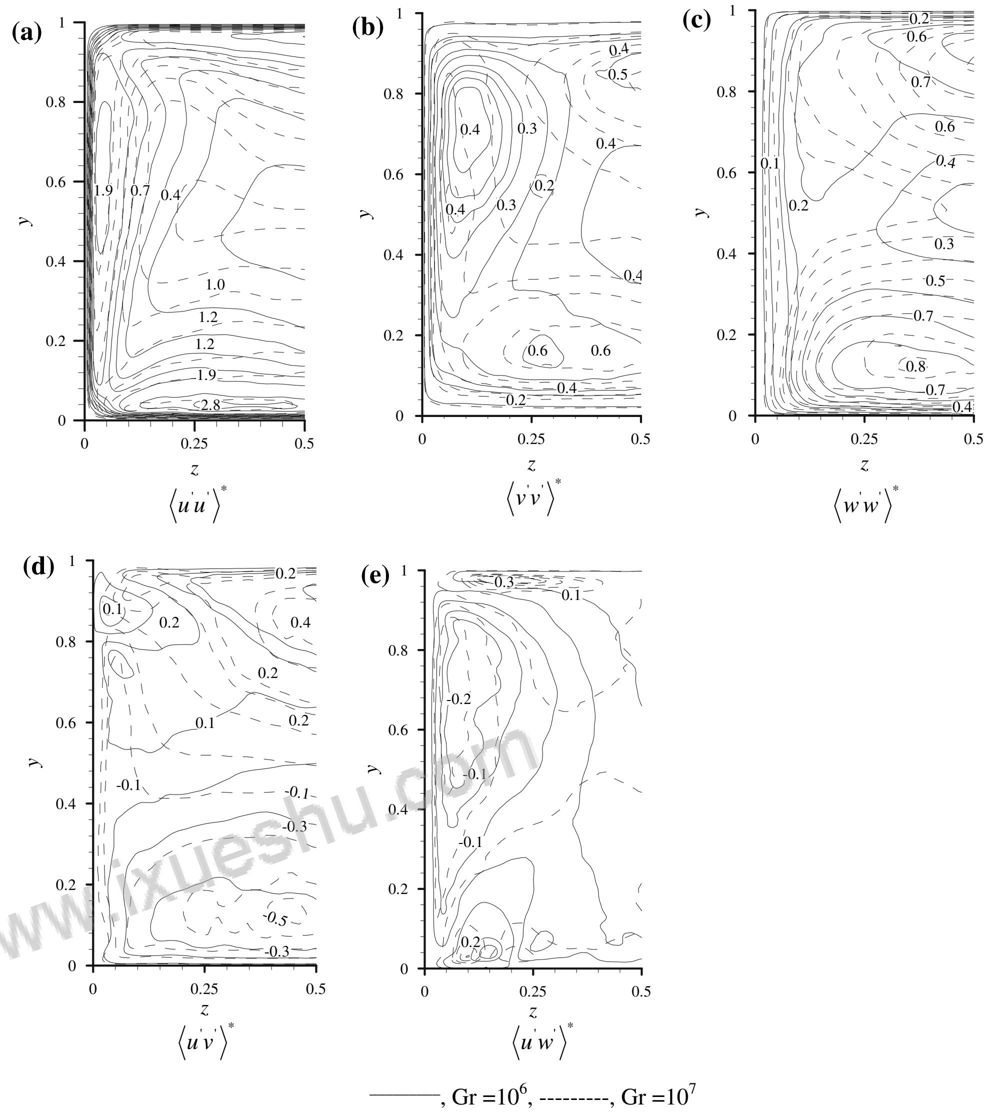

Fig. 19 Spatial distributions of Reynolds stress components in square duct flow at Re_τ = 400 for $Gr = 10^6$ (*continuous lines*) and $Gr = 10^7$ (*discontinuous lines*); **a** $< u'u' >^*$, **b** $< v'v' >^*$, **c** $< w'w' >^*$, **d** $< u'v' >^*$, **e** $< u'w' >^*$

than zero is expanded to $y = 0.8$ near the high temperature wall. The value of $| \langle u' v' \rangle^* |$ is increased and its maximum is displaced toward the high temperature wall horizontally according to the change in the distributions of $\langle v' v' \rangle^*$ in this region.

It can be seen from Fig. 18e that $\langle u' w' \rangle^*$ is similar to the distribution of $\langle u' v' \rangle^*$ so that the contour plot of $\langle u' w' \rangle^*$ can be obtained by a 90° rotation of $\langle u' v' \rangle^*$ contour plot in the (y, z)-plane for the lower Gr number. Distribution of $\langle u' w' \rangle^*$ disappears the symmetric behavior about $y = 0.5$ because of the effect of buoyancy body force (see Fig. 19e). The region where the value of $\langle u' w' \rangle^*$ is more than zero is decreased and is displaced towards the vertical wall at the down-left corner region, but at the top-left corner, the region is enlarged to $z = 0.5$. And the maximum value of $|\langle u' w' \rangle^*|$ is displaced towards the top wall near the vertical wall.

5.3 Mean streamwise momentum equation budget

Analysis of the mechanisms that affect the streamwise velocity distributions is made by examining the terms of the Reynolds-averaged streamwise momentum equation for a fully developed square duct flow, which can be written as

$$\langle v \rangle \frac{\partial \langle u \rangle}{\partial y} + \langle w \rangle \frac{\partial \langle u \rangle}{\partial z} = -\frac{\partial \langle u'v' \rangle}{\partial y} - \frac{\partial \langle u'w' \rangle}{\partial z} - \frac{d\langle p \rangle}{dx} + \frac{1}{Re_\tau}\left(\frac{\partial^2 \langle u \rangle}{\partial y^2} + \frac{\partial^2 \langle u \rangle}{\partial z^2}\right) \tag{25}$$

The terms on the left hand-side of Eq. 25 represent contribution of convection, and the terms on the right hand-side of Eq. 25 are responsible from left to right, for turbulent transport, pressure gradient and viscous diffusion, respectively. In this non-dimensional equation, u_τ and H are used as the velocity and length scales respectively. Equation 25 is averaged in both the homogeneous x-direction and in time, so all the x- and t-derivatives terms vanish except for pressure gradient, which is the constant driving pressure gradient.

The spatial distributions of the different terms in Fig. 20a and b for $Gr = 10^4$ are qualitatively the same as that reported by Huser and Bringen [16] at the wall bisector for the non-thermally-generated turbulent duct flow. All the budget terms were calculated directly as they appear in Eq. 25. At $Gr = 10^4$, along the wall bisector, the sum of the primary Reynolds shear stresses gradient balances the imposed streamwise pressure gradient in the central region of the square duct. Close to the bottom wall (Fig. 20a) and vertical wall (Fig. 20b), the primary Reynolds shears gradient ($-\partial\langle u'v'\rangle/\partial y$ near the bottom wall and $-\partial\langle u'w'\rangle/\partial z$ near the vertical wall) balances the viscous diffusion term. And diffusion effects contribute to the loss of momentum while the Reynolds stress term acts as a source in Eq. 25 favoring the transport of high momentum fluid in the central part of the duct to the wall [25]. It can be seen from Fig. 20 that, along the wall bisector, the contribution from the convection is very small, which is characterized by a relatively weak v- and w-velocity in this region.

Figure 21 shows the spatial distributions of the different terms of momentum Eq. 25 at $Gr = 10^7$. It can be seen from Fig. 21 that the Reynolds stress gradient $-\partial\langle u'v'\rangle/\partial y$ has important contribution in the central of square duct, which is balanced by the pressure gradient in this region. And the contribution from the convection increases compared to the $Gr = 10^4$. Its magnitude is 40 percent of that of Reynolds stress gradient, which is characterized by a relatively strong v- and w-velocity in this region. Figure 21b shows also that the Reynolds stress gradient and diffusion terms decrease closing to the vertical wall bisector. Toward

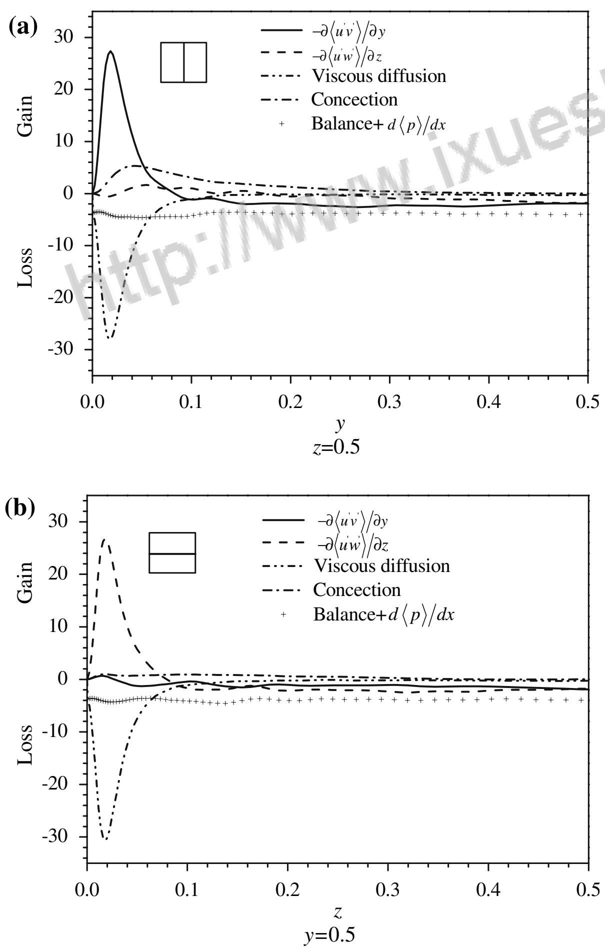

Fig. 20 Calculated x-momentum budget along the vertical and horizontal wall bisector at $Gr = 10^4$; **a** z=0.5, **b** y=0.5

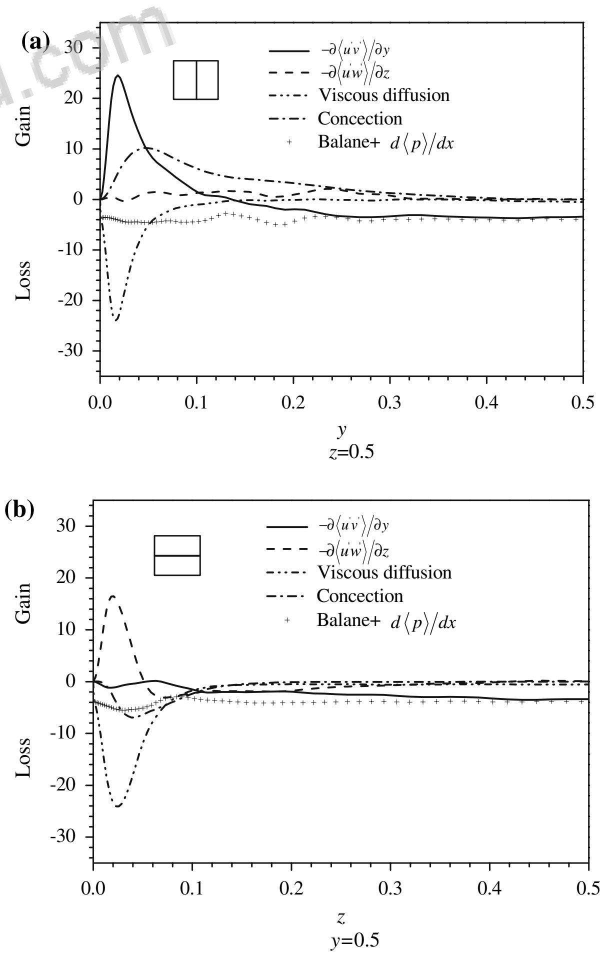

Fig. 21 Calculated x-momentum budget along the vertical and horizontal wall bisector at $Gr = 10^7$; **a** z=0.5, **b** y=0.5

the corner where the secondary velocity is stronger for $Gr = 10^4$, mean convection becomes significant. Figure 22a indicates that near the corner, mean convection balances both the viscous diffusion and the Reynolds shear stress gradient along the corner bisector. This negative convection represents a loss of u-momentum equation. The spatial distributions of the all terms for $Gr = 10^7$ are consistent with those of $Gr = 10^4$, as can be seen from Fig. 22b. Compared to the Fig. 22a, it can be seen from Fig. 22b that the contribution of convection becomes more significant at $Gr = 10^7$.

5.4 Thermal energy budget

The mechanisms that affect the averaged thermal energy distribution of the flow can be determined by examining the terms of its budget. For a fully thermally developed flow in the square duct, the thermal energy equation can be written as

$$\langle v\rangle \frac{\partial\langle\theta\rangle}{\partial y} + \langle w\rangle \frac{\partial\langle\theta\rangle}{\partial z} = -\frac{\partial\langle v'\theta'\rangle}{\partial y} - \frac{\partial\langle w'\theta'\rangle}{\partial z} + \frac{1}{PrRe_\tau}\left(\frac{\partial^2\langle\theta\rangle}{\partial y^2} + \frac{\partial^2\langle\theta\rangle}{\partial z^2}\right) \quad (26)$$

The terms on the left-hand side of Eq. 26 is convection transport, and the first and second terms on the right-hand side are turbulent transport and the third is thermal conduction. Figures 23 and 24 show the spatial distribution of the terms of the thermal budget as they appear in Eq. 26 along the vertical wall bisector and corner bisector, respectively.

It can be seen in Fig. 23a that near the vertical wall, turbulent transport is significant which balances the thermal conduction. Convection contributes a little to the overall average thermal transport at $Gr = 10^4$. Figure 23b shows that the contribution from convection becomes significant in thermal transport Eq. 26, and in the vicinity of the vertical wall convection balances both turbulent transport and thermal conduc-

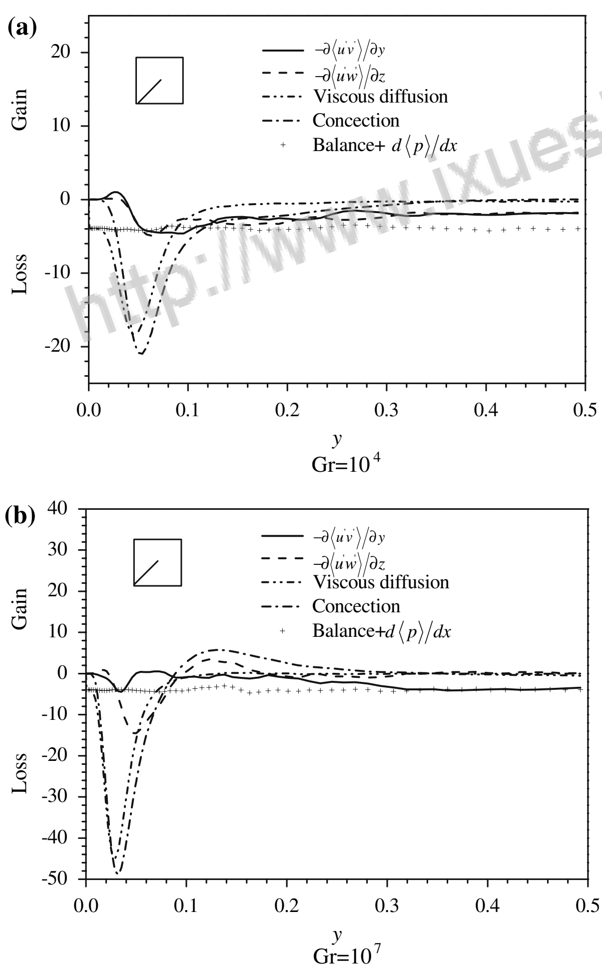

Fig. 22 Calculated x-momentum budget along corner wall bisector at $Gr = 10^4$ and $Gr = 10^7$; **a** $Gr = 10^4$, **b** $Gr = 10^7$

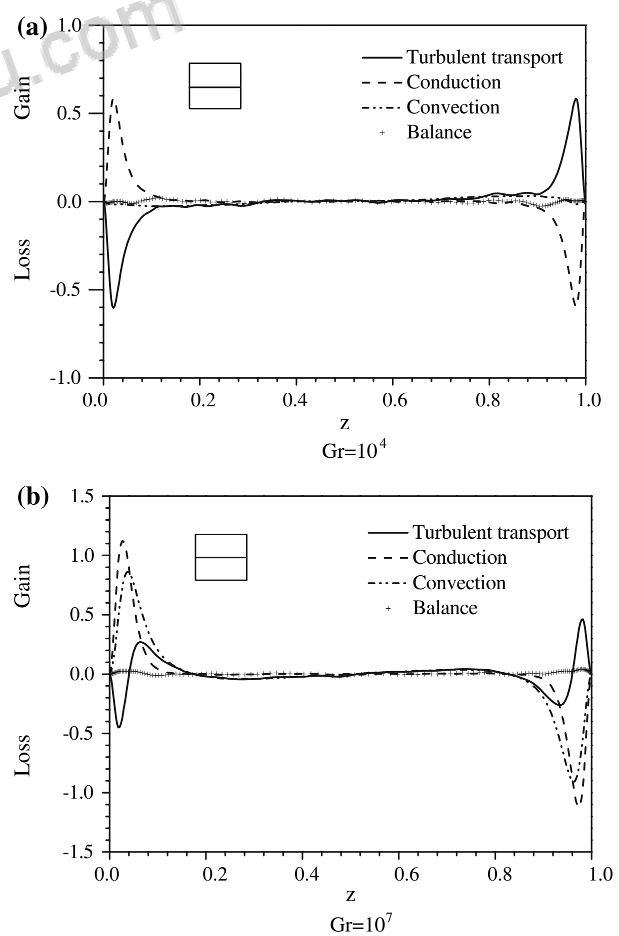

Fig. 23 Thermal energy budgets along vertical wall bisector at $Gr = 10^4$ and $Gr = 10^7$; **a** $Gr = 10^4$, **b** $Gr = 10^7$

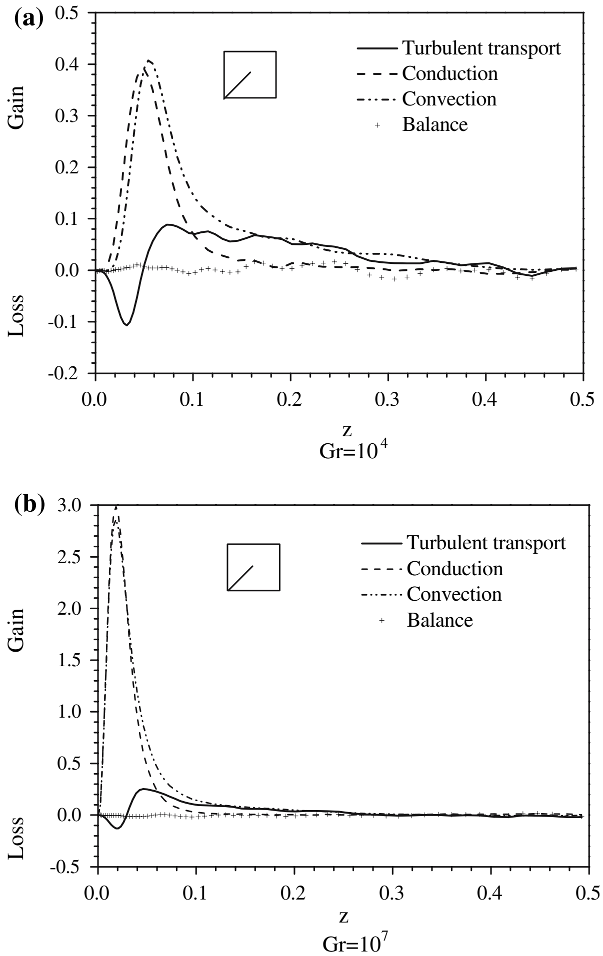

Fig. 24 Thermal energy budgets along corner bisector at $Gr = 10^4$ and $Gr = 10^7$; **a** $Gr = 10^4$, **b** $Gr = 10^7$

tion. At $Gr = 10^7$, the turbulent transport decreases compared to the $Gr = 10^4$. As can be seen from Fig. 23a and b that the dimensionless value of turbulent transport is more than 0.5 at $Gr = 10^4$, but less than 0.5 at $Gr = 10^7$, because the turbulent intensity decreases in this region. Heat conduction contributes as a source in Eq. 26 near the high temperature wall because the temperature is higher at the wall than in the fluid. On the contrary, it acts as a sink near the cold wall.

Near the corner, it can be seen in Fig. 24 that the turbulent transport and convection help to decrease the corner temperature because the secondary velocity is strong along the corner bisector [26]. And the advection is dominant compared with the turbulent transport, whose contribution in the energy Eq. 26 is only 25 percent that of convection at $Gr = 10^4$, and is 10 percent at $Gr = 10^7$. In the central region of duct, turbulent transport acts as a transport term between hot fluid close to the corner and cold fluid in the center of the duct. In this region, the turbulent transport is similar to the thermal conduction in that it decreases the temperature gradient. With the increase of *Gr* number, convection and turbulent transport increase near the corner.

6 Conclusion

In view of the lack of DNS results for the flow and temperature fields for the combined the forced convection and natural convection, in this work, DNS of the fully developed turbulent flow and heat transfer for $Re_\tau = 400$ with natural convection in the square duct has been performed. Based on our results, following observations can be obtained:

1. The high order difference scheme can obtain satisfactory accuracy in the coarse mesh, and second order central difference for the pressure Poisson equation can be used, which is economical for solving it in MPI parallel programming language environment.
2. For the lower *Gr* number ($Gr \leq 10^4$) the vortices structure has no visible change in the vector contour in the cross section, indicating Reynolds stresses owing to turbulent motion are strong compared with buoyancy force. With the increase of the *Gr* number, the buoyancy force enlarges, and the flow in the cross section gradually exhibit natural convection characteristics. However, the development of natural convection is suppressed strongly by the Reynolds stresses at $Gr = 10^7$.
3. When *Gr* number is less than 10^5 the mean heat transfer coefficient is almost constant because the secondary flow owing to the turbulent motion is dominant. For the higher *Gr* number, the mean heat flux increases with the increase of *Gr*, but it is less than that of the laminar flow with the same *Gr* number because natural convection is somewhat depressed by the Reynolds stresses.
4. The turbulent transport is important for the mean streamwise momentum and equations for the lower *Gr* number (10^5). With the increase of *Gr* number, the contribution from convection transport in the equations become significant near the wall or near the corner in the duct.

Acknowledgments The authors are gratefully to the financial support by the National Natural Science Foundation of China (nos. 50476046, 50636050), and they also greatly appreciate for the support of Shanghai Supercomputer Center (China) in using its high performance computing facilities and technical support.

References

1. Piller M, Nobile E (2002) Direct numerical simulation of turbulent heat transfer in a square duct. Int J Numer Methods Heat Fluid Flow 12:658–686
2. Demuren AO, Rodi W (1984) Caluculation of turbulence-driven secondary motion in non-circular ducts. J Fluid Mech 140:189–222
3. Brundett E, Bainesm W D (1964) The production and diffusion of vorticity in duct flow. J Fluid Mech 19:375–394
4. Lounder B E, Ying W M (1972) Secondary flows in ducts of square cross-section. J Fluid Mech 54:289–295
5. Gessner FB, Emery AF (1981) The numerical prediction of developing turbulent flow in rectangular ducts. J Fluids Eng 103:445–455
6. Lounder BE, Ying WM (1973) Prediction of flow and heat transfer in ducts of square cross-section. Proc Inst Mech Eng 187:455–461
7. Speziale CG (1987) On nonlinear k–l and k–ε models of turbulence. J Fluid Mech 178:450–475
8. Naji H, Yahyaoui O, Mompean G (2004) A priori analysis of explicit algebraic stress models for a turbulent flow through a straight square duct. American Society of Mechanical Engineers, Pressure Vessels and Piping Division (Publication) PVP, Part 1 485(1):19–25
9. Pettersson Reif BA, Andersson HJ (2002) Prediction of turbulence-generated secondary mean flow in a square duct. Flow Turbulence Combustion 68(1):41–61
10. Kajishima T, Miyake Y (1992) A discusision on eddy viscosity models on the basis of the large eddy simulation of turbulent flow in a square duct. Comput Fluids 21(2):151–161
11. Madabhushi PK, Vanka SP (1991) Large eddy simulation of turbulence-driven secondary flow in a square duct. Phys Fluids A3 11:2734–2745
12. Su MD, Friedrich R (1994) Investigation of fully developed turbulent flow in a straight duct with large eddy simulation. J Fluids Eng 116: 677–684
13. O'Sullivan PL, Biringen S, Huser A (2001) *A priori* evaluation of dynamic subgrid models of turbulence in square duct flow. J Eng Math 40: 91–108
14. Viswanathan AK, Tafti DK (2006) Detached eddy simulation of turbulent flow and heat transfer in a two-pass internal cooling duct. Int J Heat Fluid Flow 27(1):1–20
15. Gavrilakis S (1992) Numerical simulation of low-Reynolds number turbulent flow through a straight square duct. J Fluid Mech 244:101–129
16. Huser A, Biringen S (1993) Direct numerical simulation of turbulent flow in a square duct. J Fluid Mech 257:65–95
17. Sharma G, Phares DJ (2006) Turbulent transport of particles in a straight square duct. Int J Multiphase Flow 32(7):823–837
18. Kasagi N, Nishimura M (1996) Direct numerical simulation of combined forced and natural turbulent convection in a vertical plane channel. Int J Heat Fluid flow 18:88–99
19. Abe H, Kawamura H, Matsuo Y (2001) Direct simulation of a fully developed turbulent channel flow with respect to the Reynolds number dependence. Trans ASME J Fluids Eng 123:382–393
20. Lele SK (1997) Compact finite difference schemes with spectral-like solution. J Comput Phys 103:16–42
21. Friedrich R, Huttl T J, Manhart M, Wagner C (2001) Direct numerical simulation of incompressible turbulence flows. Comput Fluids 30:555–579
22. Yu B, Kawaguchi Y (2004) Direct numerical dimulation of viscoelastic drag-reducing flow: a faithful finite difference method. J Non-Newtonian Fluid Mech 116:431–466
23. Rai MM (1991) Direct simulation of turbulent flow using finite-difference schemes. J Comput Phys 96:15–53
24. Dean DB (1978) Reynolds number dependence of skin friction and other bulk flow variables in two-dimensional rectangular duct flow. ASME J Fluids Eng 100:215–223
25. Pallares J, Davidson L (2000) Large-eddy simulations of turbulent flow in a rotating square duct. Phys Fluids 12:2878–2894
26. Pallares J, Davidson L (2002) Large-eddy simulations of turbulent heat transfer in stationary and rotating square duct. Phys Fluids 14:2804–2816